A Letter of Intent on Nuclear and Particle Physics Experiments at the J-PARC 50 GeV Proton Synchrotron

An Experimental Search for A $\mu^- - e^-$ Conversion at Sensitivity of the Order of 10^{-18} with a Highly Intense Muon Source: PRISM

The PRISM/PRIME Group

April 28th, 2006

The PRISM/PRIME Group

Masaharu Aoki, Shinya Araki, Yasushi Arimoto, Imam Hossain, Takahisa Itahashi, Yasutoshi Kuriyama, Yoshitaka Kuno*, Noriyuki Miyamoto, Toshiyuki Oki, Akira Sato, Yosuke Takubo, and Makoto Yoshida
Department of Physics, Graduate School of Science, Osaka University.

Chihiro Ohmori
Accelerator Laboratory, High Energy Accelerator Research Organization (KEK),

Tatsushi Nakamoto, Toru Ogitsu, and Akira Yamamoto
Cryogenics Science Center, High Energy Accelerator Research Organization (KEK),

Yoichi Igarashi, Shigeru Ishimoto, and Koji Yoshimura
Institute of Particle and Nuclear Studies, High Energy Accelerator Research Organization (KEK),

Noboru Sasao
Department of Physics, Kyoto University,

Yoshihisa Iwashita
Accelerator Laboratory, Institute for Chemical Research, Kyoto University,

Yoshiharu Mori
Kyoto University Reactor Research Institute, Kyoto University,

Robert Palmer
Brookhaven National Laboratory,

The $*$ mark indicates the contact persons.

Contents

Chapter 1

Executive Summary

Physics Motivation : Flavor violation of charged leptons (c-LFV) has large potential for discovery. It is known that various theoretical models beyond the Standard Model predict possible existence of c-LFV at the range where future experiments could reach. Examples of such models are supersymmetric grand unification models (SUSY-GUT), supersymmetric seesaw models (SUSY-Seesaw) and a model of extra dimensions, and many others.

Among many systems to study c-LFV, the muon is superb since a number of muons available is the most. The number of muons available at present is an order of 10^{15} muons/year, and it is anticipated to have more like $10^{18} - 10^{19}$ muons/year for a new high intensity muon source called PRISM that we propose, in conjunction with the J-PARC 50-GeV proton synchrotron.

Among many muon c-LFV processes, a $\mu^- - e^-$ conversion process is the best. The other process such as $\mu^+ \to e^+\gamma$ will be seriously limited by accidental backgrounds. However, for $\mu^- - e^-$ conversion, the detector resolution is not a critical issue, rather a beam would be issue. Once a good muon beam suitable for the search for $\mu^- - e^-$ conversion, a much better experiment can be carried out.

PRISM/PRIME : PRISM is such a new-generation muon-beam source, with high intensity, high luminosity and high purity. PRISM stands for "`Phase Rotated Intense Slow Muon source`". The aimed muon beam intensity is about $10^{11} - 10^{12}$ $\mu^{\pm}$/sec, three to four orders of magnitude higher than that available at present. High luminosity can be achieved by a novel technique of phase rotation, which accelerates slow muons and decelerates fast muons by a radio frequency (RF) field. High purity, in particular small pion contamination of the level of 10^{-20}, can be achieved by a long flight length of beam particles so that almost all pions decay out.

PRIME (PRISM Mu E) is an experiment to search for $\mu^- - e^-$ conversion at an ultimate sensitivity of $B(\mu^- + A \to e^- + A) < 10^{-18}$ with a muon beam from PRISM. By using a curved solenoid spectrometer with high resolution electron detection, the sensitivity goal proposed would be possible.

The discovery potential for PRISM/PRIME is very high. If a $\mu^- - e^-$ conversion processes is found with PRISM/PRIME, this would indicate a clear signal of physics beyond the Standard Model.

Chapter 2

Charged Lepton Flavor Violation

2.1 Introduction

Recently, flavor violation of charged-leptons (c-LFV)[1] has attracted much interest from theorists and experimentalists in particle physics, since it has growing potential to find an important clue of new physics beyond the Standard Model [1]. Some of the notable features on the c-LFV studies are that (1) c-LFV might have sizable contributions from new physics, which could be observable in future experiments, and (2) c-LFV does not have any sizable Standard Model contribution (such as from neutrino mixing), which could become serious background otherwise.

Historically, the search for c-LFV was initiated by Hincks and Pontecorvo in 1947 [2]. Since then, the searches for c-LFV have been continuously carried out with various elementary particles, like muons, taus, kaons and others. The upper limits have been improved at a rate of two orders of magnitude per decade, as seen in Fig. 2.1.

The muon system is one of the best places to search for c-LFV [1]. The upper limits of various c-LFV decays are listed In Table 2.1, where it is seen that the sensitivity to c-LFV is superb in the muon system. It is mostly because of a large number of muons available for experimental searches today (of about $10^{14} - 10^{15}$ muons/year). And more muons (of about $10^{18} - 10^{19}$ muons/year) would be available in future if a new highly intense muon source (such as PRISM) is realized.

2.2 Physics Motivations

In the minimal Standard Model, lepton flavor conservation is built in by hand with assuming vanishing neutrino masses. However, neutrino mixing has been experimentally confirmed by the discovery of neutrino oscillation. Now, lepton flavor conservation is known to be violated. However, c-LFV has yet been observed experimentally. It is known that the contribution of neutrino mixing to c-LFV is extremely small, since it is proportional to $(m_\nu/m_W)^4$, yielding the order of 10^{-50} in branching ratios. Therefore, discovery of c-LFV would imply clearly new physics beyond "neutrino os-

[1] It is also called charged-lepton mixing.

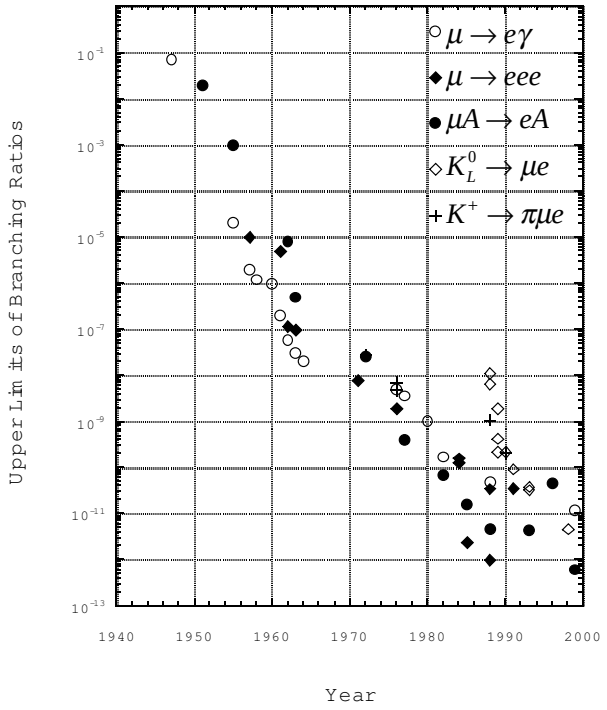

Figure 2.1: History of searches for c-LFV in muon and kaon decays

Table 2.1: Limits of the lepton-flavor violating decays of muon, tau, pion, kaon and Z boson.

Reaction	Present limit	Reference
$\mu^+ \to e^+\gamma$	$< 1.2 \times 10^{-11}$	[3]
$\mu^+ \to e^+e^+e^-$	$< 1.0 \times 10^{-12}$	[4]
$\mu^- Ti \to e^- Ti$	$< 6.1 \times 10^{-13}$	[5]
$\mu^+e^- \to \mu^-e^+$	$< 8.3 \times 10^{-11}$	[6]
$\tau \to e\gamma$	$< 3.9 \times 10^{-7}$	[7]
$\tau \to \mu\gamma$	$< 3.1 \times 10^{-7}$	[8]
$\tau \to \mu\mu\mu$	$< 1.9 \times 10^{-7}$	[9]
$\tau \to eee$	$< 2.0 \times 10^{-7}$	[9]
$\pi^0 \to \mu e$	$< 8.6 \times 10^{-9}$	[10]
$K_L^0 \to \mu e$	$< 4.7 \times 10^{-12}$	[11]
$K^+ \to \pi^+\mu^+e^-$	$< 2.1 \times 10^{-10}$	[12]
$K_L^0 \to \pi^0\mu^+e^-$	$< 3.1 \times 10^{-9}$	[13]
$Z^0 \to \mu e$	$< 1.7 \times 10^{-6}$	[14]
$Z^0 \to \tau e$	$< 9.8 \times 10^{-6}$	[14]
$Z^0 \to \tau\mu$	$< 1.2 \times 10^{-5}$	[15]

cillation". As a matter of fact, any new physics or interaction beyond the Standard Model would predict c-LFV at some levels.

The physics motivation of c-LFV is very robust for next decade. To illustrate, let us consider two possible physics cases, depending on whether LHC find supersymmetry (SUSY), as follows.

2.2.1 Case I: LHC finds SUSY

It is known that c-LFV may have significant contributions from SUSY, if SUSY particles exist in the LHC energy range. In this case, studies of c-LFV would focus on SUSY. In SUSY models, the SUSY contributions can be presented by the slepton mass matrix ($m^2_{\tilde{l}}$), given in Eq. (2.1).

$$m^2_{\tilde{l}} = \begin{pmatrix} m^2_{\tilde{e}\tilde{e}}, \Delta m^2_{\tilde{e}\tilde{\mu}}, \Delta m^2_{\tilde{e}\tilde{\tau}} \\ \Delta m^2_{\tilde{\mu}\tilde{e}},\ m^2_{\tilde{\mu}\tilde{\mu}}, \Delta m^2_{\tilde{\mu}\tilde{\tau}} \\ \Delta m^2_{\tilde{\tau}\tilde{e}}, \Delta m^2_{\tilde{\tau}\tilde{\mu}},\ m^2_{\tilde{\tau}\tilde{\tau}} \end{pmatrix} \tag{2.1}$$

The SUSY contributions to c-LFV depend on an off-diagonal element $\Delta m^2_{\tilde{\mu}\tilde{e}}$ or $\Delta m^2_{\tilde{e}\tilde{\mu}}$.[2] Therefore, the determination of these SUSY contributions would enable us to study the slepton mass matrix and therefore SUSY (soft) breaking. In the following, the SUSY contributions to c-LFV is presented in more details.

In minimum SUSY models, charged lepton mixing would occur through mixing of their corresponding sleptons. Fig.2.2 shows one of the SUSY diagrams contributing to muon to electron transition, where the mixing of smuon ($\tilde{\mu}$) and selectron ($\tilde{e}$) is given by an off-diagonal slepton mass matrix $\Delta m^2_{\tilde{\mu}\tilde{e}}$. In minimum SUSY models, the slepton mass matrix is assumed to be a diagonal matrix at the Planck mass scale (10^{19} GeV), and no off-diagonal matrix elements exits ($\Delta m^2_{\tilde{\mu}\tilde{e}} = 0$). Then, non-zero off-diagonal matrix elements can be induced by radiative corrections from the Planck scale to the weak scale ($\sim 10^2$ GeV). There could be two scenarios at high energy

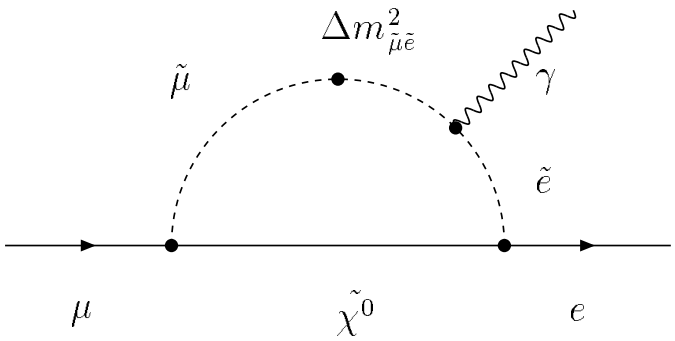

Figure 2.2: One of the diagrams of SUSY contributions to a μ to e transition. $\Delta m^2_{\tilde{\mu}\tilde{e}}$ indicates the magnitude of the slepton mixing.

[2]Similarly, the SUSY contributions to the muon $g-2$ and the muon EDM are a real and an imaginary parts of the diagonal element $m^2_{\tilde{\mu}\tilde{\mu}}$, respectively.

to induce off-diagonal elements of the slepton mass matrix. One is grand unification (GUT) where the GUT Yukawa interaction creates non-zero off-diagonal elements. This scenario is called **SUSY-GUT** models. And the other is Seesaw mechanism, where the neutrino Yukawa interaction does. This is called **SUSY-Seesaw** models. Both of the models predict the branching ratios of c-LFV from just below to a few orders of magnitude below the current experimental upper limits. Therefore, if we could improve experimental sensitivity by a few orders of magnitude, this would provide great discovery potential.

2.2.1.1 SUSY-GUT

IIn SUSY-GUT, the non-zero slepton mixing appears unavoidably through radiative corrections in the renormalization group evolution from the GUT scale to the weak energy scale [16]. It is given by

$$\Delta m^2_{\tilde{\mu}\tilde{e}} \propto \frac{3m_0^2 + A_0^2}{8\pi^2} h_t^2 V_{td}^* V_{ts} \ln \frac{M_{GUT}}{M_{R_3}} \tag{2.2}$$

where m_0 is the universal scalar mass. V_{td} and V_{ts} are the Kobayashi-Maskawa (KM) quark mixing matrix elements. Recently, it was pointed out that the slepton mixing thus generated is very large owing to the large top-quark Yukawa coupling [17]. The branching ratios of $\mu^- - e^-$ conversion predicted in SUSY SU(5) models [1] are shown in Fig. 2.3. They range from 10^{-15} to 10^{-13} for the singlet smuon mass of $m_{\tilde{\mu}_R}$ of 100 to 300 GeV [18]. They are larger for a large $\tan\beta$ value. The SO(10) SUSY GUT models give an even larger value of 10^{-13} to 10^{-11} by an enhancement of $(m_\tau^2/m_\mu^2) \sim 100$ [17]. It is because of the existence of loop diagrams whose magnitude is proportional to the tau-lepton mass in SO(10) SUSY-GUT models.

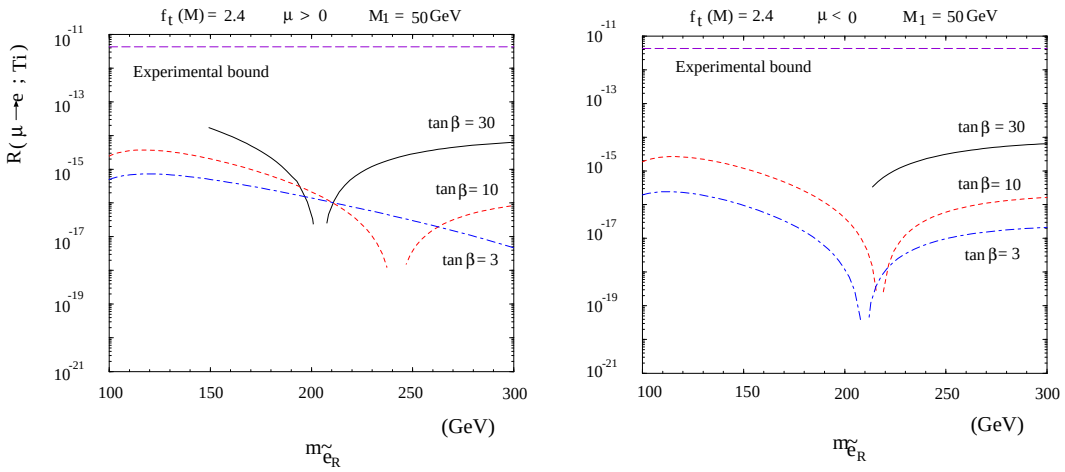

Figure 2.3: Predicted branching ratios for $\mu^- - e^-$ conversion in SUSY-GUT.

2.2.1.2 SUSY-Seesaw

The other model is supersymmetric models with the seesaw mechanism, which predict the existence of right-handed heavy neutrinos. As widely known, there is experimental evidence for the existence of neutrino masses and their mixing. In the SUSY model with the seesaw mechanism, the slepton mixing can be induced from the neutrino mixing. Then, c-LFV processes in muon decays are also expected to occur [19, 20, 21]. In principle, there can be potentially two contributions to the slepton mixing $\Delta m^2_{\tilde{\mu}\tilde{e}}$. One is from $U_{\mu e}$ corresponding to the solar neutrino mixing. The other is from the product of $U_{\tau e}$ and $U_{\tau\mu}$ that corresponds to the atmospheric neutrino mixing. Assuming the tau Yukawa coupling is large, the second contribution can be large. In this case, the slepton mixing can be given by

$$\Delta m^2_{\tilde{\mu}\tilde{e}} \propto \frac{3m_0^2 + A_0^2}{8\pi^2} h_\tau^2 U^*_{\tau e} U_{\tau\mu} \ln \frac{M_{GUT}}{M_{R_3}} \tag{2.3}$$

where $U_{\tau e}$ and $U_{\tau\mu}$ are the Maki-Nakagawa-Sakata (MNS) neutrino mixing matrix elements. h_τ is the tau Yukawa coupling. The prediction is shown in Fig.2.4.

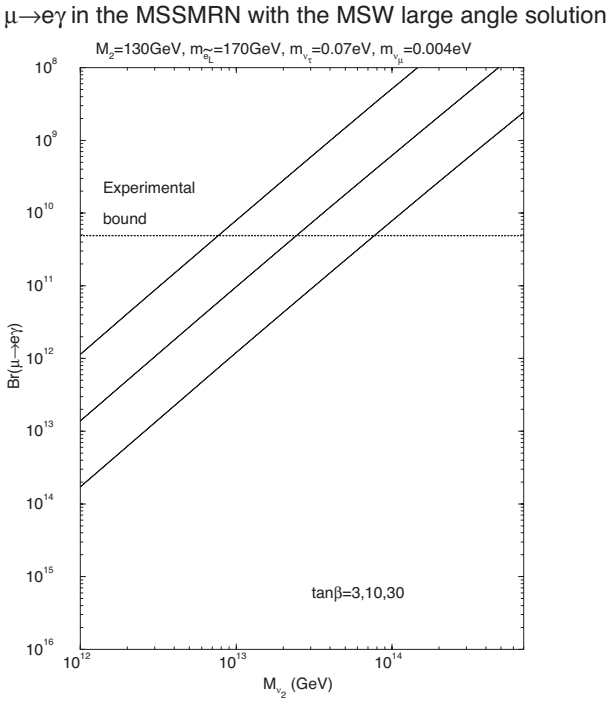

Figure 2.4: Predictions of $\mu^+ \to e^+\gamma$ branching ratio in SUSY-Seesaw models. The three lines correspond to the cases of $\tan\beta = 30, 10, 3$ respectively.

Fig.2.5 shows the two possible mechanisms to make slepton mixing in MSSM (supergravity SUSY). In SUSY-GUT cases, the slepton mixing is given by the product of the KM matrix elements, while in SUSY-Seesaw cases, it is given by the product of the MNS matrix elements. When LHC finds SUSY, charged lepton mixing attract

more interest, in terms of studying either SUSY-GUT or SUSY-Seesaw models, rather than just minimum SUSY itself.

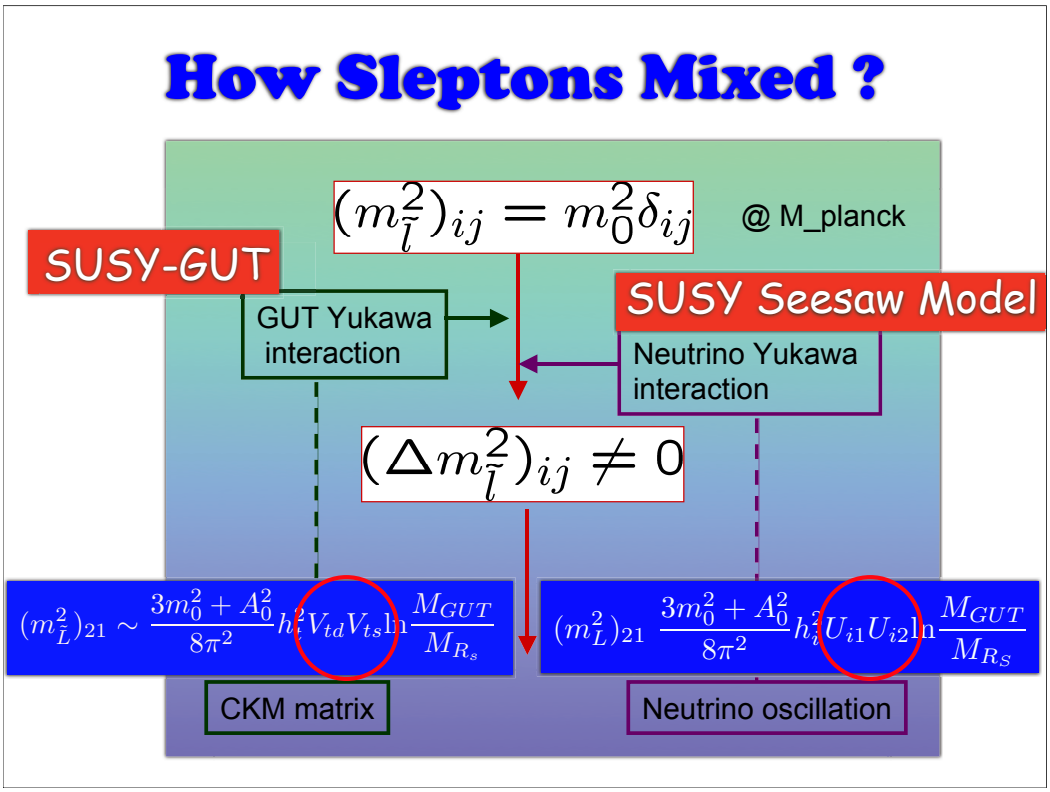

Figure 2.5: Two physics mechanisms (SUSY-GUT and SUSY-Seesaw) to introduce the slepton mixing in the MSSM.

2.2.2 Case II: LHS does not find SUSY

When LHC does not find SUSY, two cases can be considered; either no SUSY at all or heavier SUSY at multi TeV scale. High precision frontier with intense slow muons comes to the forefront, since it is sensitive to heavier mass scale than that high-energy accelerators can reach. For c-LFV, besides SUSY, there are other models to predict c-LFV, such as heavy neutrino models, leptoquark models, composite, two Higgs doublet models, second Z' models, anomalous Z coupling, and so on.

For heavier SUSY, if the c-LFV search has sufficient experimental sensitivity (such as 10^{-18} for $\mu^- - e^-$ conversion), it is sensitive to the SUSY mass scale up to several TeV, as shown in Fig.2.6. And thereby the search for c-LFV would be worth to carry out even if LHC does not find SUSY below TeV energy scale.

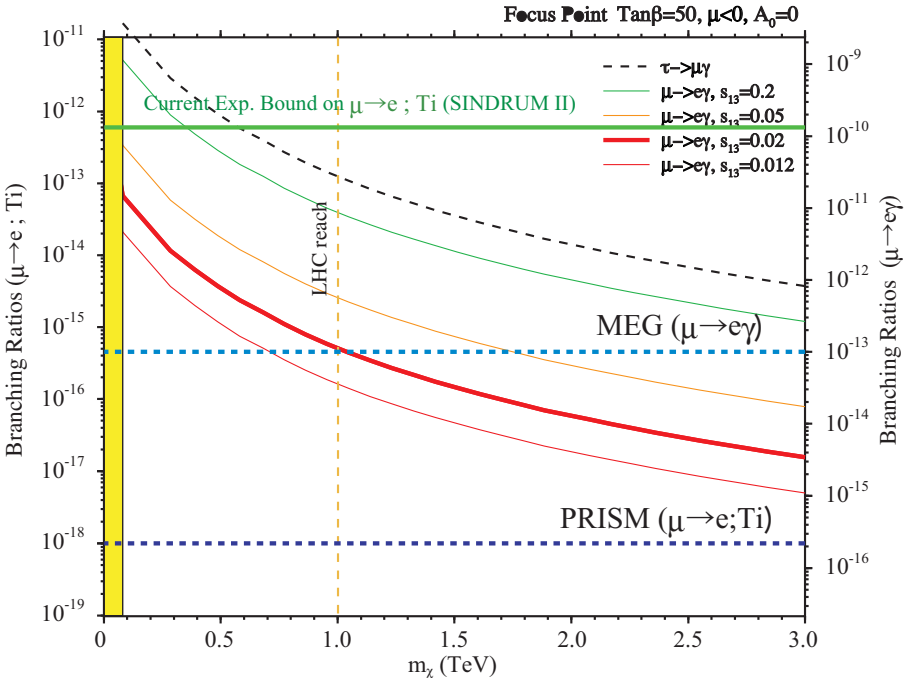

Figure 2.6: Prediction of the branching ratio of MEC in Ti in SUSY-Seesaw models as a function of SUSY mass scale (neutralino). The PRISM sensitivity is also shown.

2.3 Phenomenology of $\mu^- - e^-$ Conversion

2.3.1 What is a $\mu^- - e^-$ Conversion Process ?

One of the prominent muon LFV process is $\mu^- - e^-$ conversion in a muonic atom. When a negative muon is stopped in some material, it is trapped by an atom, and forms a muonic atom. After it cascades down in energy levels in the muonic atom, a muon is bound in its $1s$ ground state. The fate of the muon is then either decay in an orbit ($\mu^- \to e^- \nu_\mu \overline{\nu}_e$) or capture by a nucleus of mass number A and atomic number Z, namely

$$\mu^- + (A, Z) \to \nu_\mu + (A, Z - 1). \tag{2.4}$$

However, in the context of physics beyond the Standard Model, the exotic process of neutrinoless muon capture, such as

$$\mu^- + (A, Z) \to e^- + (A, Z), \tag{2.5}$$

is also expected. This process is called $\mu^- - e^-$ conversion in a muonic atom. It violates the conservation of the lepton flavor numbers, L_e and L_μ, by one unit, but conserves the total lepton number, L.

The branching ratio of $\mu^- - e^-$ conversion can be given by

$$B(\mu^- + (A,Z) \to e^- + (A,Z)) \equiv \frac{\Gamma(\mu^- + (A,Z) \to e^- + (A,Z))}{\Gamma(\mu^- + (A,Z) \to capture)}, \qquad (2.6)$$

where Γ is the corresponding decay width.

The final state of the nucleus (A, Z) could be either the ground state or excited states. In general, the transition process to the ground state, which is called coherent capture, is dominant. The rate of the coherent capture process over non-coherent ones is enhanced by a factor approximately equal to the number of nucleons in the nucleus, since all of the nucleons participate in the process.

2.3.2 Event Signature

The event signature of the coherent $\mu^- - e^-$ conversion in a muonic atom is a mono-energetic single electron emitted from the conversion with an energy of

$$\begin{aligned} E_{\mu e} &= m_\mu - B_\mu - E^0_{rec} \\ &\approx m_\mu - B_\mu, \end{aligned} \qquad (2.7)$$

where m_μ is the muon mass, and B_μ and E^0_{rec} are the binding energy of the $1s$ muonic atom and the nuclear-recoil energy respectively. The nuclear-recoil energy is approximately $E^0_{rec} \approx (m_\mu - B_\mu)^2/(2M_A)$, where M_A is the mass of the recoiling nucleus, which is small. Since B_μ is different for various nuclei, the peak energy of the $\mu^- - e^-$ conversion signal changes. For instance, it varies from $E_{\mu e} = 104.3$ MeV for titanium to $E_{\mu e} = 94.9$ MeV for lead.

From an experimental point of view, $\mu^- - e^-$ conversion is very attractive. Firstly, the e^- energy of about 105 MeV is far above the end-point energy of the muon decay spectrum ($\sim$ 52.8 MeV). Secondly, since the event signature is a mono-energetic electron, no coincidence measurement is required. The search for this process has the potential to improve the sensitivity by using a high muon rate without suffering from accidental background, which would be serious backgrounds for other processes, such as $\mu^+ \to e^+\gamma$ and $\mu^+ \to e^+e^+e^-$ decays.

2.3.3 $\mu^- - e^-$ conversion and $\mu^+ \to e^+\gamma$

As explained later, there could be two contributions in the $\mu^- - e^-$ diagrams. One is a photonic contribution, and the other is a non-photonic contribution. For the photonic contribution, there is some relation between the $\mu^- - e^-$ conversion process and the $\mu^+ \to e^+\gamma$ decay. Suppose a photonic contribution is dominant, the branching ratio of the $\mu^- - e^-$ conversion process is expected be smaller than that of $\mu^- - e^-$ decay by a factor of α, namely about a few hundred. It implies that the search for $\mu^- - e^-$ conversion at the level of 10^{-16} is comparable to that for $\mu^+ \to e^+\gamma$ at the level of 10^{-14}.

More precisely, this factor depends on the nucleus used in the $\mu^- - e^-$ conversion search[22]. For instance, the factor in Ti is about 1/250 the branching ratio of $\mu^+ \to e^+\gamma$. With taking account of relativistic atomic effects, Coulomb distortion, finite nuclear size and nucleon distribution, it was found that the ratio of $\mu - e$ conversion to $\mu^+ \to e^+\gamma$ varies from 1/389 for ^{27}Al to 1/238 for ^{48}Ti, and decreases again to 1/342 for ^{208}Pb [23].

If the non-photonic contribution dominates, there is no relation between $\mu^+ \to e^+\gamma$ decay and $\mu^- - e^-$ conversion. It would be worth to note the following. When a $\mu^+ \to e^+\gamma$ signal is found, then a $\mu^- - e^-$ conversion signal has to be found. When no $\mu^+ \to e^+\gamma$ signal is found, there is still opportunity to find a $\mu^- - e^-$ conversion signal if non-photonic contribution exits.

Regarding the non-photonic contribution, it is argued that an extra logarithmic enhancement of the photonic loop diagrams for $\mu^- - e^-$ conversion (and also $\mu^+ \to e^+e^-e^+$) over $\mu^+ \to e^+\gamma$ has also been discussed [24]. It happens only when light charged fermions, to which a photon is attached, are involved in the loop diagrams. Therefore, it could occur for SUSY models with R-parity breaking, but not for R-parity conserving SUSY models or SUSY-GUT models.

2.3.4 Present Status of the Searches

In this subsection, the present status of the LFV experiments with muons in particular, the searches for $\mu^- - e^-$ conversion and $\mu^+ \to e^+\gamma$ decay are presented.

2.3.4.1 Experimental status of $\mu^- - e^-$ conversion

Table 2.2 summarizes a history of $\mu^- - e^-$ conversion in various nuclei.

Table 2.2: History and summary of $\mu^- - e^-$ conversion in various nuclei.

Process	90% C.L. upper limit	place	year	reference
$\mu^- + Cu \to e^- + Cu$	$< 1.6 \times 10^{-8}$	SREL	1972	[31]
$\mu^- + {}^{32}S \to e^- + {}^{32}S$	$< 7 \times 10^{-11}$	SIN	1982	[32]
$\mu^- + Ti \to e^- + Ti$	$< 1.6 \times 10^{-11}$	TRIUMF	1985	[33]
$\mu^- + Ti \to e^- + Ti$	$< 4.6 \times 10^{-12}$	TRIUMF	1988	[34]
$\mu^- + Pb \to e^- + Pb$	$< 4.9 \times 10^{-10}$	TRIUMF	1988	[34]
$\mu^- + Ti \to e^- + Ti$	$< 4.3 \times 10^{-12}$	PSI	1993	[35]
$\mu^- + Pb \to e^- + Pb$	$< 4.6 \times 10^{-11}$	PSI	1996	[28]
$\mu^- + Ti \to e^- + Ti$	$< 6.1 \times 10^{-13}$	PSI	1998	[5]

The SINDRUM II collaboration at PSI had carried out experiments to search for $\mu^- - e^-$ conversion in various nuclei. A schematic view of the SINDRUM II spectrometer is shown in Fig. 2.7. It consisted of a set of concentric cylindrical drift chambers inside a superconducting solenoid magnet of 1.2 T. Negative muons with a momentum of about 90 MeV/c were stopped in a target located at the center of

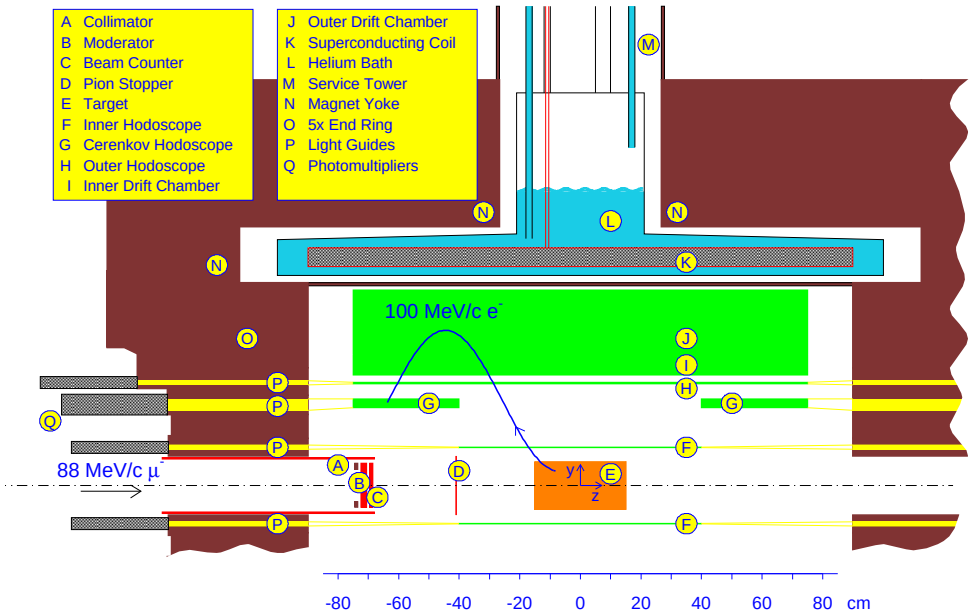

Figure 2.7: Schematic layout of the SINDRUM-II detector.

the apparatus, after passing a CH_2 moderator and a beam counter made of plastic scintillator. Charged particles with transverse momentum (with respect to the magnetic field direction) above 80 MeV/c, originating from the target, first hit two layers of plastic scintillation arrays followed by two layers of drift chambers, before eventually hitting plexiglass Cherenkov hodoscopes placed at both ends. Charged particles having transverse momentum below about 80 MeV/c were contained inside, and could not reach the tracking region under a magnetic field of 1.2 T. A momentum resolution of about 2.8% (FWHM) for the energy region of conversion electrons was achieved. For the background rejection the following are used in an off-line analysis: the e^- energy (E_e), a time delay between the times of charged particle tracks in the spectrometer and the beam-counter signal (Δt), the position of the origin of the reconstructed trajectory (Δz) and the polar track angle. Events with small Δt were removed so as to reject prompt backgrounds, such as electron scattering and radiative pion capture.

In a 1993 run with a titanium target, a total of 3×10^{13} stopped μ^-s were accumulated at a rate of 1.2×10^7 μ^-/s from the $\mu E1$ beam line at PSI. The overall efficiency was about 13 %. The e^- momentum spectrum for the Ti target in the 1993 data is shown in Fig. 2.8, where the successive background rejections by prompt veto (*i.e.* Δt cut) and cosmic-ray suppression are shown. Since no events were found in the signal region, a 90% C.L. upper limit of 6.1×10^{-13} was obtained [5]. Also, for a lead target, it gave $B(\mu^- Pb \rightarrow e^- Pb) < 4.6 \times 10^{-11}$ [28]. Following this work, SINDRUM-II took data with a gold target and those with a lead target in 1997 and

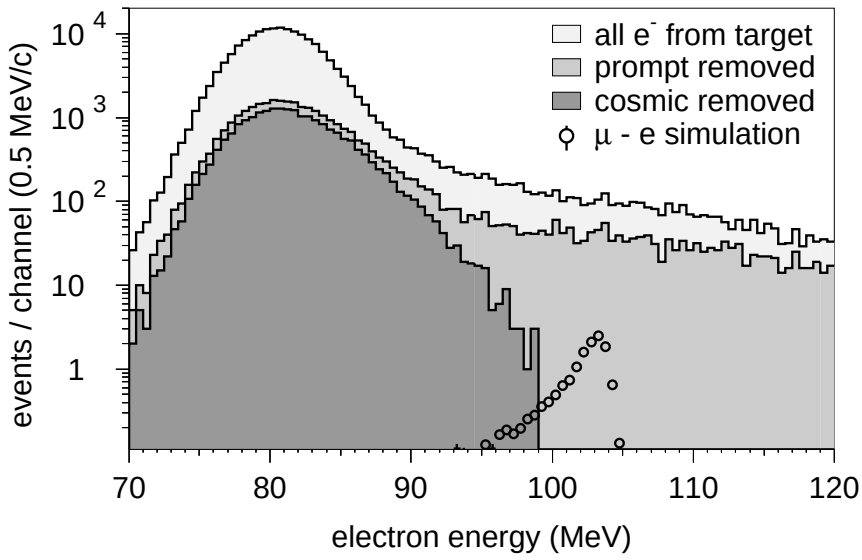

Figure 2.8: Electron momentum distribution for the $\mu^- + Ti \rightarrow e^- + Ti$ reaction, measured by the SINDRUM-II detector.

1998, respectively. The data analysis is underway.

A new experiment (E940) at Brookhaven National Laboratory (BNL) AGS, called the MECO (Muon Electron COnversion) experiment, was prepared [29]. MECO aims to search for $\mu^- + Al \rightarrow e^- + Al$ at a sensitivity below 10^{-16}. But, it was unfortunate that the MECO experiment was announced to be cancelled due to budget problems in summer, 2005.

2.3.4.2 Experimental Status of $\mu^+ \rightarrow e^+\gamma$ Decay Search

A experimental search for $\mu^+ \rightarrow e^+\gamma$ was carried out by the MEGA collaboration at Los Alamos National Laboratory (LANL). The MEGA detector consisted of a magnetic spectrometer for the positron and three concentric pair-spectrometers for the photon. They were placed inside a superconducting solenoid magnet of a 1.5 T field. The positron spectrometer comprised eight cylindrical wire chambers and scintillators for timing. The positron energy resolution (FWHM) was from 0.5 MeV (0.95%) to 0.85 MeV (1.6%) for a 52.8-MeV e^+, depending on the number of helical loops of e^+ tracks. For the pair-spectrometer, each layer had lead converters, MWPCs, drift chambers and scintillators. The photon energy resolutions (FWHM) were 1.7 MeV (3.3%) and 3.0 MeV (5.7%) for the outer and inner Pb conversion layers, respectively. A surface μ^+ beam of 29.8 MeV/c was introduced along the detector axis, and was stopped in the muon-stopping target made of a thin tilted Mylar foil. All of the charged particles from muon decays were confined within the positron spectrometer. The intensity of the muon beam was 2.5×10^8/sec with a macroscopic duty factor of 6%. The total number of muons stopped was 1.2×10^{14}. By using the likelihood

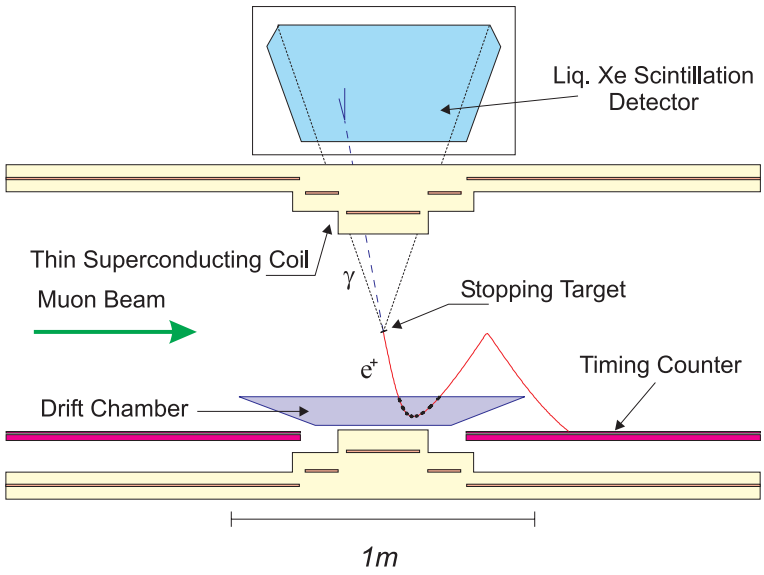

Figure 2.9: Schematic layout of the MEG detector.

method, a new limit of 1.2×10^{-11} with 90% C.L. has been reported [3].

A new experiment called MEG at PSI, which aims at a sensitivity of 10^{-14} in the $\mu^+ \to e^+\gamma$ branching ratio, is under construction[36]. A schematic view of the detector is shown in Fig.fg:meg. The improvement will be expected by utilizing a continuous muon beam of 100% duty factor at PSI. With keeping the same instantaneous beam intensity as MEGA, the total number of muons available can be increased by a factor of 16. Further improvement is a novel liquid xenon scintillation detector of the "Mini-Kamiokande" type, which is a 0.8-m^3 volume of liquid xenon viewed by an array of a total of 800 photomultipliers from all the sides. The expected resolutions (FWHM) of the photon energy and position are about 1.4% and 4 mm, respectively. As the e^+ detection, a solenoidal magnetic spectrometer with a graded magnetic field is adopted, in which the magnetic field is arranged so that e^+ from the $\mu^+ \to e^+\gamma$ decay follows a trajectory with a constant radius, independently of its emission angle. It allows easier identification of the e^+ in the $\mu^+ \to e^+\gamma$ decay. Physics data taking is expected to start in year 2004 or later.

Chapter 3

Overview of The Experiment

3.1 Why is a $\mu^- - e^-$ conversion ?

Considering its remarkable physics importance, it is highly desirable to consider a next-generation experiment to search for c-LFV. There are three physics processes to be considered; namely $\mu^+ \to e^+\gamma$, $\mu^+ \to e^+e^+e^-$, and $\mu^- - e^-$ conversion.

The three processes have different experimental issues to improve their experimental sensitivities. They are summarized in Table 3.1. The processes of $\mu^+ \to e^+\gamma$ and $\mu^+ \to e^+e^+e^-$ are detector-limited. To consider and go beyond the present sensitivities (and presently-aimed sensitivities), detection resolutions have to be improved. And it is in general very hard. In particular photon energy resolution (which is involved in $\mu^+ \to e^+\gamma$ search) is difficult. On the other hand, for $\mu^+ \to e^+\gamma$ conversion, there is no accidental background and an experiment with higher rates can be doable if a new muon source, which has a higher beam intensity and has a better beam quality to suppress any beam-associated backgrounds, can be constructed.

Table 3.1: c-LFV processes and issues

Process	Major backgrounds	Beam requirements	Sensitivity Issues
$\mu^+ \to e^+\gamma$	accidentals	DC beam	detector resolution
$\mu^+ \to e^+e^+e^-$	accidentals	DC beam	detector resolution
$\mu^- - e^-$ conversion	beam-associated	pulsed beam	beam

Furthermore, it is known that compared with $\mu^+ \to e^+\gamma$. $\mu^- - e^-$ conversion and $\mu^+ \to e^+e^+e^-$ have more physics process to contribute to. Even in SUSY models, the photon-mediated diagrams can contribute to all the three processes, but the Higgs-mediated diagrams can contribute to only $\mu^- - e^-$ conversion and $\mu^+ \to e^+e^+e^-$. In summary, a search for $\mu^- - e^-$ conversion would be a natural next step to go beyond for future improvement.

3.2 A Proposed $\mu^- - e^-$ Conversion Experiment

From the reasons mentioned above, we are planning to carry out a new experiment, which aims at an ultimate sensitivity of 10^{-18} in the process of $\mu^- + Ti \rightarrow e^- + Ti$ at J-PARC. To achieve this goal, we have to construct a new muon beam source as well as a new spectrometer. In particular, improvement of a muon source is mandatorySuch improvements could be possible if we construct a muon beam with high intensity, high luminosity and high purity, together with a high-resolution spectrometer.

The requirements for a muon beam with high intensity, high luminosity, and high purity for a $\mu^- - e^-$ conversion could be summarized as follows.

- **A Muon Beam with High Intensity**: An ultimate sensitivity achievable in searches for rare processes can be limited by a number of muons available. Therefore, a highly intense beam is essential. The muon beam intensity of $10^{11} - 10^{12}$ μ^-/sec can be considered with novel technique of a muon source combined with a Mega-watt proton machine. It would yield about more than $10^{20}\mu^-$ per year.

- **A Muon Beam with High Purity**: Beam contaminations, in particular, are necessary to be reduced to remove any background associated with them. It is already shown that the past experiments like SINDRUM-II have already seen one background event just above the signal region, and they suspect that it came from a pion contaminated in a beam, through radiative pion capture. Therefore, it is the most important to reduce pion contamination in a beam.

- **A Muon Beam with Narrow Energy Width**: Narrow energy spread of the beam will allow a thin muon stopping target to improve the momentum resolution of e^- detection, which is limited by energy loss in the muon stopping target.

To achieve such a muon beam source, we have considered the PRISM muon beam source. In addition to PRISM, we have considered a new spectrometer (called PRIME). They are shown in Fig.3.1. Each of those will be explained in the following sections.

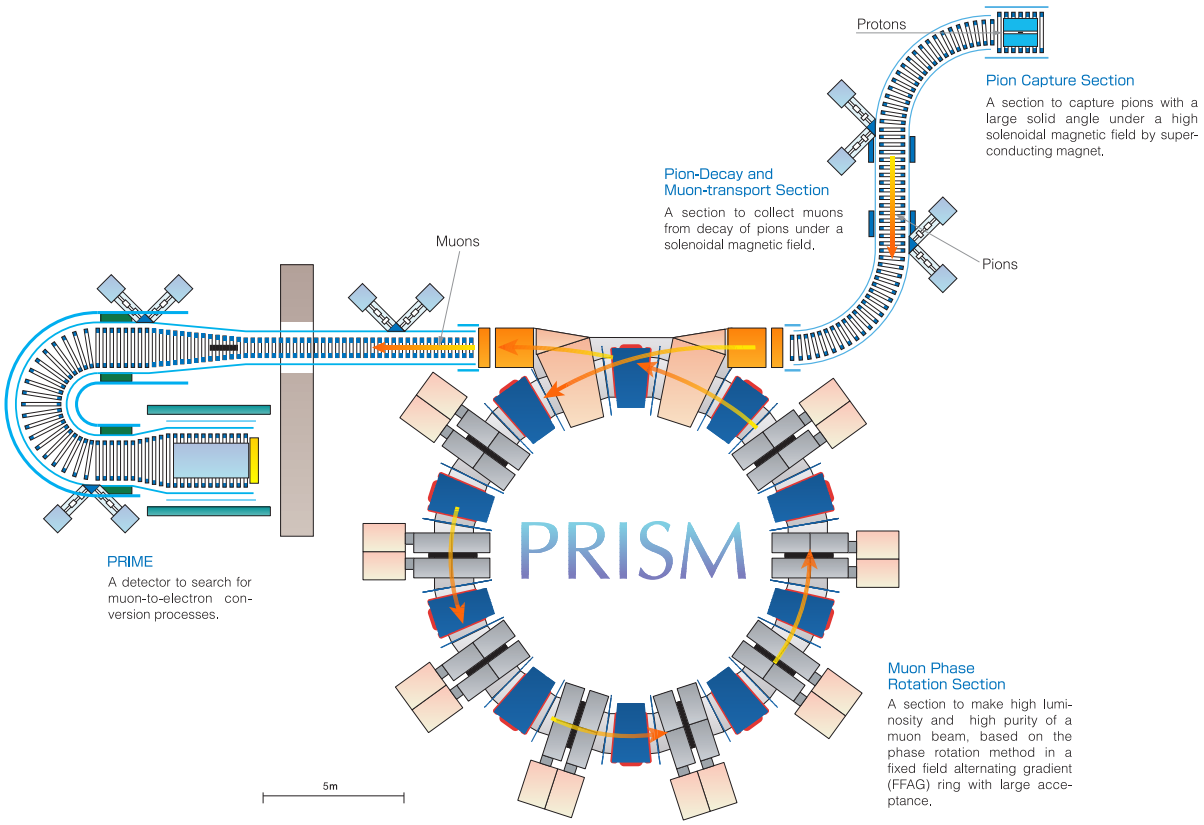

Figure 3.1: Schematic layout of PRISM with a curved solenoid spectrometer for the $\mu^- - e^-$ conversion experiment : PRIME.

Chapter 4

The PRISM Beam

In order to achieve the aimed experimental sensitivity of $\sim 10^{-18}$, not only the quantity (high intensity) of a muon beam but also its qualities, such as monochromaticity and purity are critical. We propose to provide a muon beam dedicated to the $\mu^- - e^-$ conversion experiment. In this chapter, a brief overview of the PRISM beam is presented.

4.1 Overview

PRISM is a project to provide a dedicated source of a high intensity muon beam with narrow energy-spread and small beam contamination. PRISM stands for "*Phase Rotated Intense Slow Muon source*". The aimed beam intensity is $10^{11} - 10^{12} \mu^{\pm}$/sec, four orders of magnitude higher than that available at present. It is achieved by large solid-angle pion capture with a high solenoid magnetic field. The narrow energy spread can be achieved by phase rotation, which accelerates slow muons and decelerates fast muons by an radio frequency (RF) field. The pion contamination in a muon beam can be removed by a long flight path of beam particles in PRISM so that most of pions decay out.

PRISM consists of

- a pulsed proton beam (to produce a short pulsed pion beam),
- a pion capture system (with large-solid angle by a high solenoidal magnetic field),
- a pion decay and muon transportation system (in a long solenoid magnet of about 10 m long), and,
- a phase rotation system (which accelerates slow muons and decelerates fast muons by an RF field),

A schematic layout of PRISM is shown in Fig. 3.1. One of the features of PRISM is to do phase rotation by a Fixed-Field Alternating Gradient synchrotron (FFAG), which has several advantages, such as large momentum acceptance. Some of the

key components are explained in detail in the following sections. The PRISM beam characteristics are summarized in Table 4.1.

Table 4.1: Anticipated design characteristics of the PRISM beam

Parameters	Design goal	Comments
Beam Intensity	$10^{11} - 10^{12}\mu^{\pm}$/sec	10^{14} protons/sec is assumed.
Muon kinetic energy	20 MeV	$P_{\mu} = 68$ MeV/c
Kinetic energy spread	$\pm(0.5 - 1.0)$ MeV	
Beam Repetition	100 - 1000 Hz	

4.2 Protons in the 50-GeV Ring

4.2.1 Proton Beam Power and Time Structure

A number of pions (and therefore their daughter, muons) produced by a proton beam is proportional to proton-beam power which is given by the product of its beam energy and its beam current. Roughly speaking, as long as the beam power is the same, the pion yield would be almost the same. It is based on the fact that the pion cross section increases linearly as proton beam energy. At the initial stage of PRISM, beam power of 0.67 MW (40 GeV and 16.7 μA) is assumed at the initial stage.[1]

The time structure of protons is critical for phase rotation. PRISM would require a pulsed proton beam produced by fast extraction, since phase rotation needs muons (and therefore their parents, pions) to be within a narrow time spread before phase rotation[2]. If a time spread of the muon beam is larger, the energy spread after phase rotation becomes worse. A pulse width of much less than 10 nsec is needed.

Although a pulsed proton beam from fast extraction should be used for PRISM, since there is no room in the neutrino beam line to build a dedicated experimental hall for PRISM, we would like to request the construction of a new experimental hall and a beam line for fast-extraction.

If PRISM is constructed at J-PARC, a proton beam from the J-PARC 50-GeV proton synchrotron (PS) would be used. It should be noted that a proton beam from the 3-GeV PS can not be used. The reasons are the following: (1) PRISM needs a narrow pulsed beam of protons, but in the present extraction scheme, a beam from the 3-GeV PS has a pulse width of more than 100 nsec, and (2) it is of technical difficulty to make a narrow pulse of 3 GeV since a space-charge effect, which blows a beam away, is more severe at lower energy, and (3) in the present muon-science facility, a full target (of about 1-2 interaction lengths) can not be placed since it is located upstream from the neutron scattering facility in the same proton beam line.

[1] It will be adopted to accommodate future proton upgrade of 4MW, where the target issue has to be such as a liquid mercury jet target being developed at a neutrino factory R&D.

[2] The details of phase rotation will be described in Chapter 4.5.

4.2.2 Bunch Operation

At the 50-GeV proton synchrotron, the beam intensity of 3.3×10^{14} proton per cycle and a cycle time of 0.3 Hz are expected. The 50-GeV protons are extracted to the nuclear-particle (NP) experimental hall by slow extraction, and to the neutrino beam line by fast extraction. When operated in a slow extraction mode, the average beam current and the duty factor are 15 μA and 0.20 respectively.

To have the best performance of phase rotation, it is necessary to have a narrow pulse width of the proton beam. The present pulse width in the J-PARC 50-GeV proton synchrotron is 6 nsec in sigma[3].

The typical cycle structure of the J-PARC 50-GeV PS is illustrated in Fig. 4.1. Four batches (each of which contains 2 bunches) from the 3-GeV PS are injected into the 50-GeV PS ring when it stays at a low field. When 8 buckets out of 10 are filled with beams, the 50-GeV ring starts acceleration. The time period of every bunch is about 535 nsec (1.67 MHz) and a gap separation is about 300 nsec (*i.e.* 50 % filling).

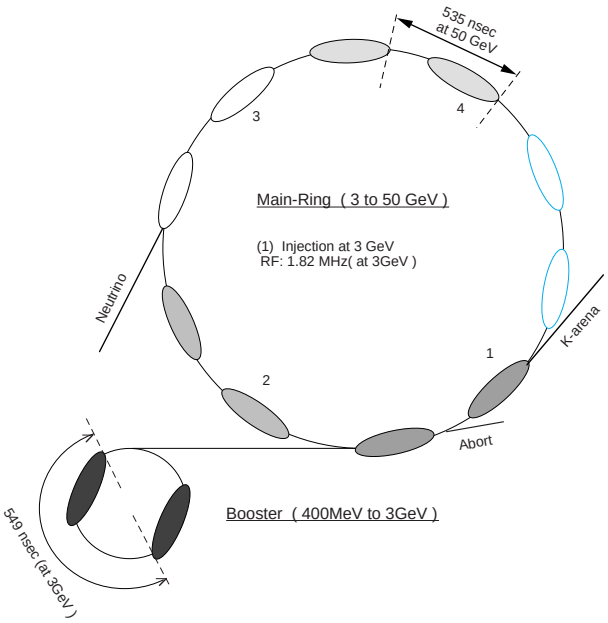

Figure 4.1: Typical machine cycle structure

4.3 Target and Capture System

The highest beam intensity in the world, which would be provided by PRISM, could be achieved by large-solid angle capture of pions at their production.

[3]The accelerator people generally use a ±3 sigma width as a full pulse width. Therefore, this case implies a full width of 36 nsec.

4.3.1 Pion Production by 50-GeV Proton Incident

PRISM would provide a low energy muon beam for stopped muon experiments, in general. Therefore, to capture, pions of low energy, which are the parent particle of the muons are of interest. At the same time, high energy pions could become potential backgrounds to eliminate. To study pion capture, simulation was performed by using both MARS and GEANT3 with FLUKA. The MARS code is a hadron production code developed at Fermilab.

Fig.4.2 shows the momentum spectra of π^- produced from a graphite target. It is seen that the maximum of transverse momentum (p_T) is around 100 MeV/c for $0 < p_L < 200$ MeV/c for both the forward and backward pions. The maximum of the total momentum for the backward pions is located at about 120 MeV/c, whereas that for the forward pions is about 200-400 MeV/c. Is is also seen that pions at high energy are suppressed in the backward direction. From these reasons, we decided to use the backward pions for PRISM.

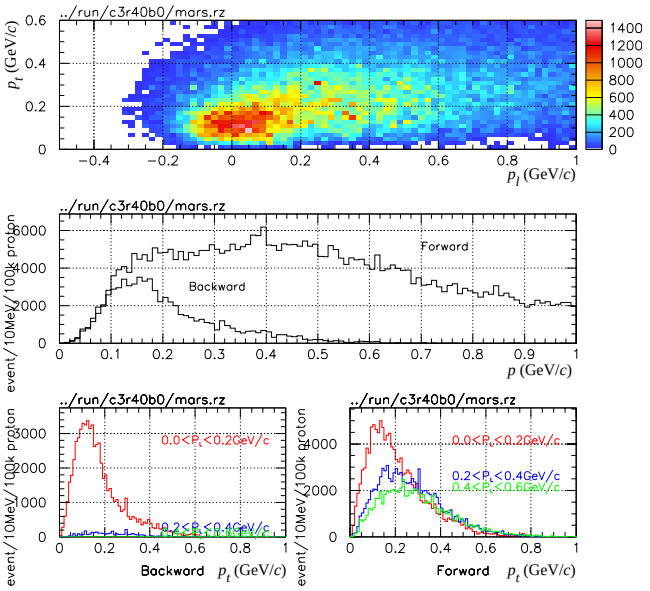

Figure 4.2: Pion production in a graphite target. (top) correlation between p_L and p_T, (middle) Total momentum distributions for forward and backward π^-s, (bottom) p_T distributions for $0 < p_L < 0.2$ GeV/c, $0.2 < p_L < 0.4$ GeV/c, and $0.4 < p_L < 0.6$ GeV/c.

4.3.2 Pion Production Target

In the baseline design of PRISM, graphite would be employed as a pion production target. A heavy material for the pion production target is better than a light material. For example, the pion yield by a tungsten target is about 3 times larger than that of a graphite target. However, heavy metal might melt down when a proton beam of 1 MW beam power hits, since it has the lower meting point. It would be however needed

to replace graphite target frequently due to the radiation damage on the specific heat of graphite.

The yield of pions at low energy is almost saturated at a target length of more than 2 interaction lengths. The increase of the yield from 2 to 3 interaction lengths is very small, of about 10%. Both a heavy and a light materials show the same tendency. The yield of pions at low energy decreases as the radius of the target increases. This would be explained by the absorption of pions at low energy. The optimum radius is about 2 cm. Therefore, graphite target with the length of 2 interaction length and with the radius of 2 cm would be used in He-gas-cooled or water-cooled configration.

Alternative options, such as (1) a rotating metal band system, (2) a liquid mercury jet and (3) a tantalum fine particles packed in the titanium casing, are being studied. All these are studied in the R&D works for the neutrino factory projects in the world-wide.

4.3.3 Pion Capture Solenoid Magnet

To collect as many pions (and cloud muons) of low energy as possible, they are captured under a high solenoidal magnetic field with a large solid angle. In this case, pions emitting in a half hemisphere can be captured within the transverse momentum threshold ($p_t^{\max}$). The $p_t^{\max}$ is given by a magnetic field strength (B) and the radius of the inner bore of solenoid magnet (R) as

$$p_T^{\max}(GeV/c) = 0.3 \times B(\mathrm{T}) \times R(\mathrm{m})/2. \tag{4.1}$$

To optimize the magnetic field of the capture solenoid, the muon yields are estimated at 10 m from the target, where most of pions decay into muons in the transport solenoid magnet following the capture solenoid magnet. It was seen that the higher the pion capture magnetic field is, the better the muon yield at the exit of the pion decay system becomes. Therefore, a higher magnetic field is preferable. According to Fig.4.2, placing $p_T^{\max}$ at around 200 MeV/c would be sufficient. Furthermore, since we are interested in the muon momentum being less than 84 MeV/c, the solenoid magnet with the bore radius of 15 cm can accept most of the parent pions for such low-energy muons. Detailed optimization of the bore radius strongly depends on the available technology of the superconducting solenoid magnet. In the current design, we employ the conservative design values, namely of $B = 6$ T, $R = 15$ cm and the length of 1.4 m.

We should install radiation shield between the target and the superconducting coil. This will further increase the total radius of the superconducting solenoid magnet. The radiation heat load on superconducting coils placed behind the radiation shield of tungsten of 30 cm in length is the level of 3×10^{-3} W/g. The radiation heat come mostly from neutrons.

If copper is used as the stabilizer of the superconducting coils, a total thickness of the coil would be about 20 cm or more to generate 6-Tesla magnetic field, and a total impact on the 4.5 K refrigeration load is over 1 kW. In order to overcome this difficulty, the aluminum stabilizer would be employed since the radiation heat load

to the coil increases proportionally to its total mass. From the MARS simulation study on the radiation shielding, a thickness of the radiation shield made of tungsten should be about 30cm or more, if it is required the heat load on the superconducting coil should be less than 100 W.

4.4 Transport Solenoid

Pions and muons which were captured by the pion capture system are transported to the phase rotator in a experimental area through a transport solenoid channel. The channel consists of three sections of solenoid: a matching section, a curved section, and a decay section.

4.4.1 Matching Solenoid Section

The match between a high field capture solenoid and a low field transport solenoid would be made by gently changing the magnetic field : a matching solenoid. Although the directional distribution of the pions and muons captured at the capture system is broad, it becomes more parallel to the beam axis after the matching section. From the Liouville theorem, a volume in the phase space that beam particles occupy do not change. Under a solenoidal magnetic field, the relation between the radius of curvature (R) and the transverse momentum (p_t) leads to the relation given by

$$p_t \times R \propto \frac{p_t^2}{B} = \text{constant}, \tag{4.2}$$

where B is a magnitude of the magnetic field. Suppose the magnetic field decreases gradually, p_t also decrease, yielding a more parallel beam. This is the principle of the adiabatic transition. On the other hand, since

$$p_t \times R \propto B \times R^2 = \text{constant}', \tag{4.3}$$

the radius of curvature increase by a factor of $\sqrt{2}$. Therefore, the inner radius of a magnet in the pion decay section has to be $\sqrt{2}$ times that of the pion capture. With the cost of a beam brow up, a pion beam becomes more parallel. Furthermore, it is not effective in reality to have a long magnet with a high magnetic field, and a magnetic field has to be lowered at some point. Fig.4.3 illustrates the principle of adiabatic transition.

4.4.2 Curved Solenoid Section

To bring pions and muons into the experimental area, a beam has to be bent. Also it is necessary to make a hole in the solenoid magnets for initial protons to enter. These could be achieved by introducing a curved solenoid magnets.

It is known that a center of the helical trajectory of charged particles is drifted in a curved solenoid field. The drift (D[m]) is given by

$$D = \frac{1}{0.3 \times B} \times \frac{s}{R} \times \frac{p_l^2 + \frac{1}{2}p_t^2}{p_l} \tag{4.4}$$

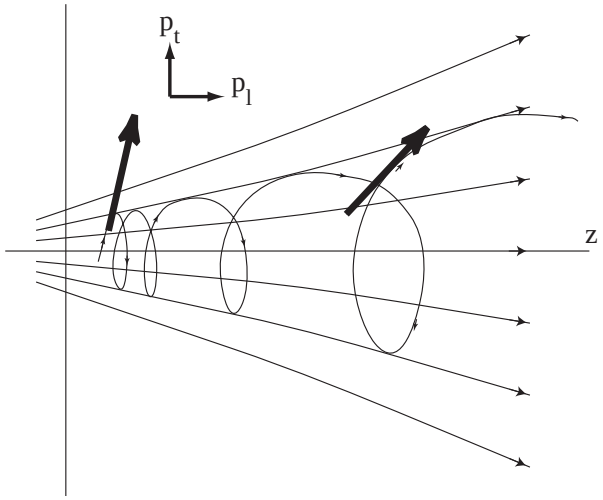

Figure 4.3: Adiabatic transition from a high magnetic field to a low magnetic field. This adiabatic transition reduces the magnitude of transverse magnetic field.

where B[T] is a magnetic field at the axis, s [m] and R[m] are a path length and the radius of curvature of a bent solenoid. Namely, s/R is a bending angle. p_l and p_t[GeV/c] are parallel and transverse momentum respectively. Charged particles with opposite sign move in the opposite direction. This can be used for charge and momentum selection if a suitable collimator is placed after the curved solenoid. This kind of curved solenoid magnets have been already adopted in the MECO (BNL-AGS E940) experiment. Unless two curved solenoid of opposite bent are installed, a dipole magnetic field to compensate a drift of the central momentum is needed.

4.4.3 Decay Solenoid Section

To let pions decay into muons, we need a long flight path. Also to contain those pions and decay muons in a limited space, a long solenoid magnet is required. At the momentum of about 100 MeV/c, a mean decay length is about 10 m, and therefore a flight length of 10 m is needed. Fig.4.4 shows the relative fractions of the pion, the muon and the electron at the exit of a 10-m solenoid magnet.

At the exit of the long solenoid magnet, a fringing field might blow up the muon distribution. This was studied by using GEANT3.21 with a fringing magnetic field calculated with POISSON/SUPERFISH. It was concluded that although most of the muons will spread out at the fringing field region, the core parts in the good emittance, which can be accepted by the PRISM-FFAG ring, would be contained within $\pm$50 cm, where the next focusing elements should capture them.

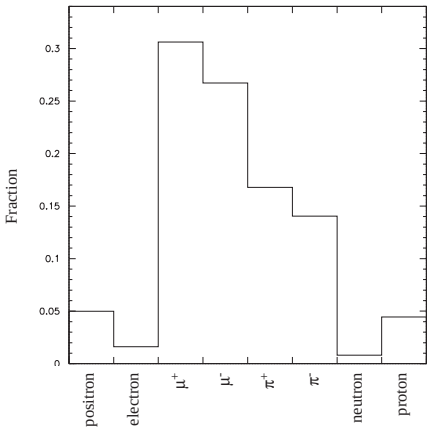

Figure 4.4: Fractions of pions, muons and electrons at the end of a 10-m long solenoid decay system.

4.5 Phase Rotation

4.5.1 Principle of Phase Rotation

Phase rotation is a method to achieve a beam of narrow energy spread. The principle of phase rotation is to accelerate slow muons and decelerate fast muons by a strong radio-frequency (RF) electric field, in order to yield narrow longitudinal momentum spread. It corresponds to 90° rotation of the phase volume occupied by muons in a beam in the energy-time phase space, as schematically shown in Fig.4.5. After phase rotation, the projection of the phase volume onto the energy axis becomes narrower and sharper. By phase rotation, the initial time spread is converted into the final energy spread. The narrow width of a pulsed proton beam is very critical for a net performance of phase rotation.

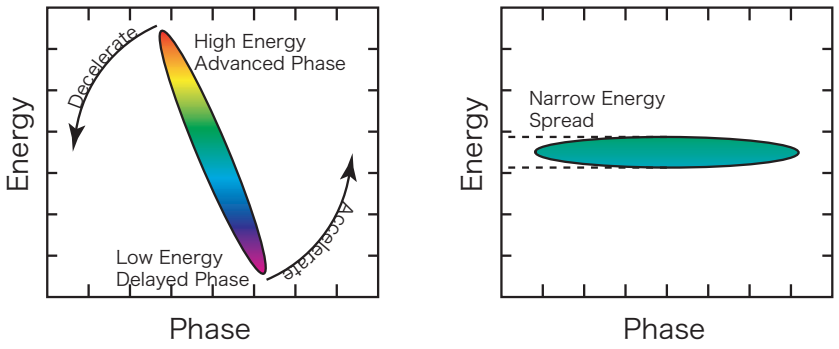

Figure 4.5: Principle of phase rotation shown in the energy-time phase space. The initial narrow time spread is converted into the final narrow energy spread.

4.5.2 PRISM-FFAG as a Phase Rotator

One of the features of the phase rotation in PRISM is to adopt a circular (ring) machine. A circular machine could have smaller and compact size, compared with a linear phase rotation system. The number of RF cavities and the required electric power is greatly reduced by a factor of the turns necessary for phase rotation. Therefore, a total cost can be significantly smaller. Among many circular machine, a Fixed-Field Alternating Gradient synchrotron(FFAG) has been selected because of (1) its capability of rapid acceleration and (2) its large longitudinal and transverse acceptance. It is called the PRISM-FFAG ring from now on.

In order to achieve a high intensity muon beam, it is necessary for the PRISM-FFAG to have both of large transverse acceptance and large momentum acceptance. Furthermore, long straight sections to install RF cavities are required to obtain a high surviving ratio of the muon. The parameters of the beam optics of the PRISM-FFAG ring and its layout are shown in Table 4.2 and Fig.4.6 respectively. The

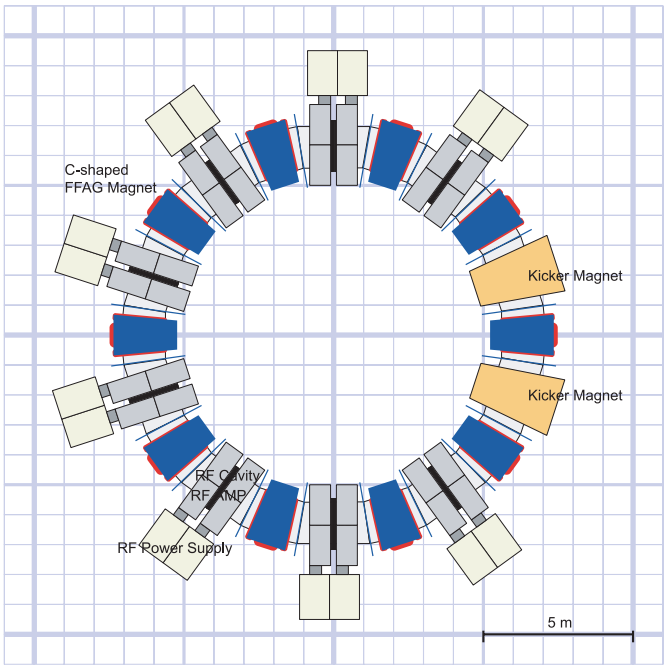

Figure 4.6: Schematic layout of the PRISM-FFAG

PRISM-FFAG ring is now under construction in Osaka university. The first three PRISM FFAG magnets are constructed, as shown in fig.4.7. The magnet has a huge aperture of 30 cm in vertical and 100 cm in horizontal. According to the tracking simulations using a magnetic field map calculated by TOSCA, PRISM-FFAG has more than about 40,000 πmm·mrad in the horizontal acceptance and about 6,500 πmm·mrad in the vertical acceptance.

Since the muon is an unstable particle (lifetime$\sim$2.2μs), it is crucial to complete phase rotation as quickly as possible in order to increase a number of surviving muons.

Table 4.2: Optics parameters of PRISM-FFAG

No. of sectors	10
Magnet type	Radial sector
	DFD triplet
	C-shaped
Field index (k-value)	4.6 (variable 4.4-5.2)
F/D ratio	6.2 (variable 4-8)
Opening angle	F/2 : 2.2deg.
	D : 1.1deg.
Aperture	H 100cm x V 30cm
Average radius	6.5m for 68MeV/c
Tune	horizontal : 2.71
	vertical : 1.52

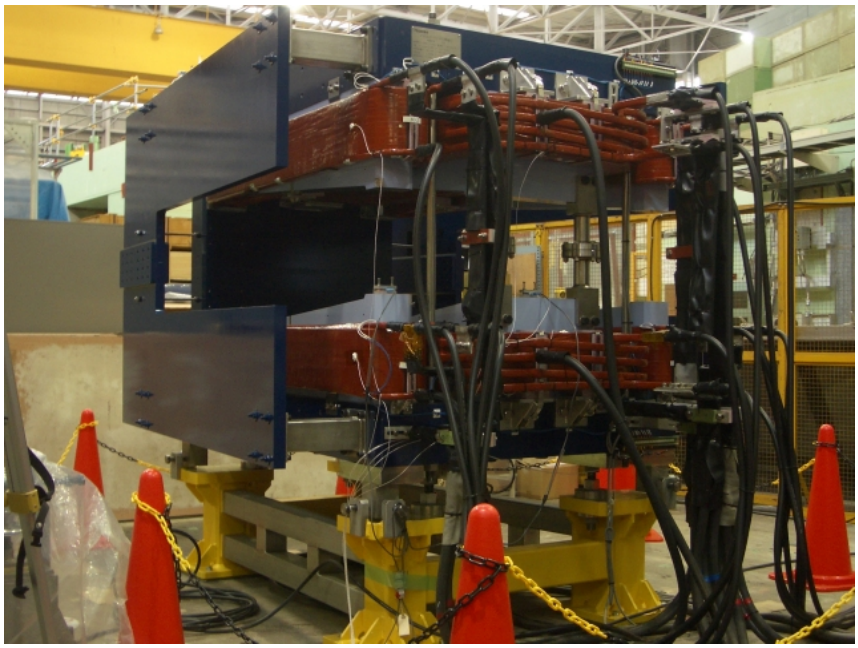

Figure 4.7: Magnet for PRISM-FFAG

PRISM requires very high field gradient of ∼170kV/m at the low frequency (4∼5 MHz). As compared with usual cavities, PRISM has to operate its cavities at a remarkably outstanding condition. We already have successfully developed such a high gradient RF system. Parameters of the RF system are summarized in Table 4.3. Figure 4.8 and Fig. 4.9 show a magnetic alloy core and a prototype RF system, which consists of an amplifier and an anode power supply and an auxiliary power supply, for PRISM-FFAG. RF voltage of ± 43kV/gap has already achieved with a test cavity, which has a shunt impedance of 735 Ω at 5MHz. It promises a field gradient with a PRISM cavity, which would have a shunt impedance of 900 Ω, to be 165kV/m. A

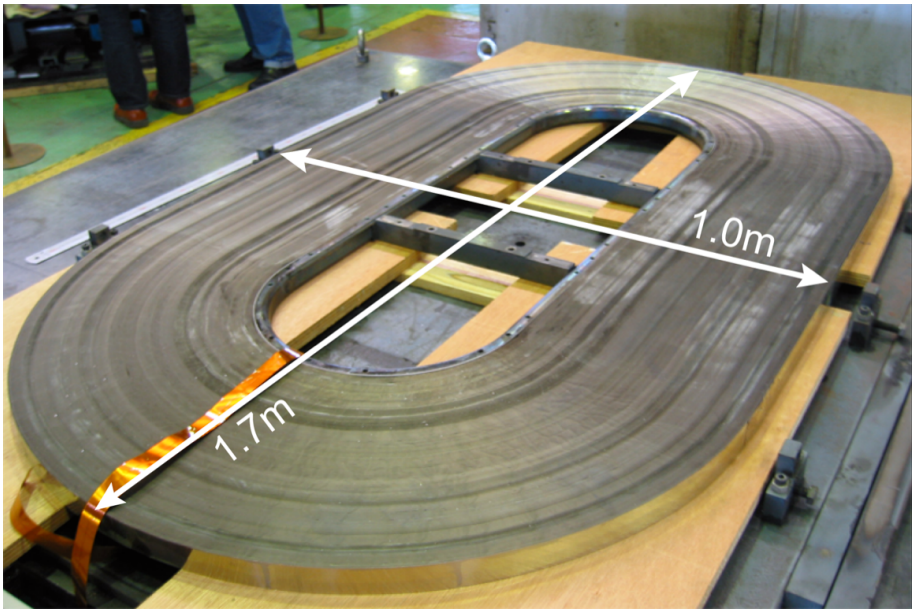

Figure 4.8: Magnet alloy core

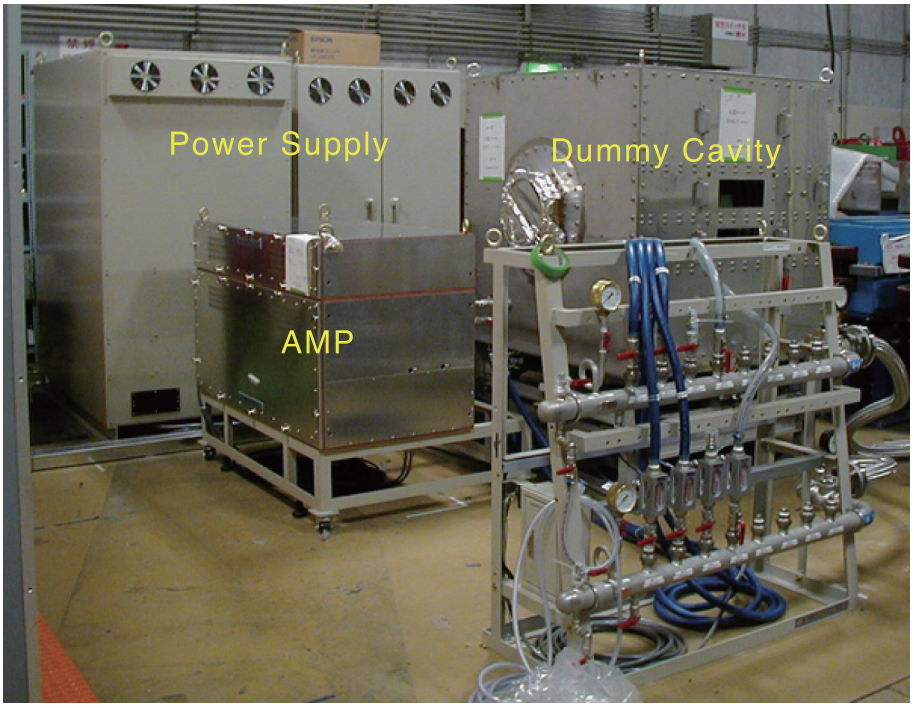

Figure 4.9: Prototype RF system

simulation result of phase rotation in PRISM-FFAG, assuming above field gradient, is shown in Fig.4.10. The initial momentum spread of 68MeV/$c\pm$ 20% is reduced to $\pm$ 2% in 6 turns (=1.5μs). A muon surviving rate is 56%.

Number of gap per cavity	5
Length	33cm/gap
Number of core per gap	6
Core material	Magnetic Alloy
Core shape	Racetrack
Core size	1.7m × 1.0m × 3.5cm
Inner aperture	1.0m × 0.3m
Shunt impedance	∼900Ω/gap
RF frequency	4∼5MHz
Field gradient	150 ∼ 200kV/m
Flux density in core	320 Gauss
Power tube	tetrode : 4CW100,000E
	plate voltage : DC33-37kV
Maximum current	60A/gap
Maximum RF power	1.5MW
Core cooling	Air cooling
Duty	<0.1%

Table 4.3: Parameters of PRISM-FFAG RF system.

4.6 Estimated Muon Yields

The muon yield (Y_μ) at PRISM can be given by

$$Y_\mu = N_p \cdot N_\pi \cdot \varepsilon_{\pi-decay} \cdot \varepsilon_{mom} \cdot \varepsilon_{time} \cdot \varepsilon_{emittance} \cdot \varepsilon_{dispersion} \cdot \varepsilon_{FFAG} \cdot \varepsilon_{\mu-decay}, \quad (4.5)$$

where N_p is a number of protons per seconds, N_π is a number of pions captured at the pion capture system per proton. ε_{mom}, ε_{time}, $\varepsilon_{emittance}$, $\varepsilon_{dispersion}$, ε_{FFAG}, $\varepsilon_{\pi-decay}$, and $\varepsilon_{\mu-decay}$ are, respectively, the momentum acceptance (50 MeV/c < P_μ < 90 MeV/c), the timing acceptance (of about ±5 nsec), the beam emittance acceptance of the PRISM-FFAG ring, the efficiency of the dispersion matching between the muon transport system and the PRISM-FFAG ring, the survival rate during 5 turns in the PRISM-FFAG, the pion decay rate, and the muon survival rate due to muon decay.

They can be estimated by using Monte Carlo simulations with the assumption of particular design based on some technologies employed. The technology choice has a large impact on the muon yield. In particular, N_π and $\varepsilon_{emittance}$ have strong dependence on the target material and length, the magnitudes of the pion capture field (capture field) and of the pion-decay and muon-transport system (transport field). Although we have not fully optimized, typical sampling cases are listed in Tables 4.4, where the numbers of muons per 10^{14} 40-GeV protons per second (J-PARC 0.6MW) and 4.4×10^{14} 50-GeV protons per second (J-PARC 4MW) are shown[4]. In this estimation, the 3-interaction target length of 120 cm and of 28.8 cm for

[4]At 4 MW beam power (4×10^{14} protons per second), it is known that the solid targets, like graphite and tungsten, might not be able to be used. Several alternatives are discussed such as a mercury liquid jet, a rotating band target, a tantalum fine-particle target.

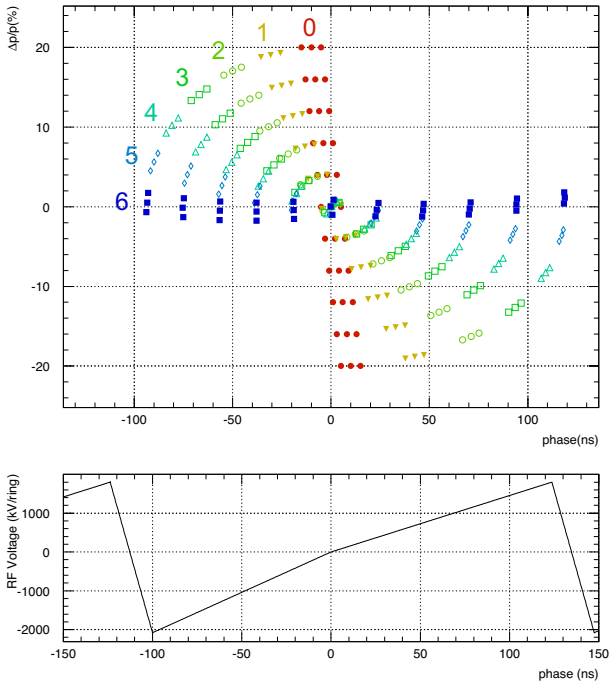

Figure 4.10: A result of simulation of phase rotation in the PRISM-FFAG ring. 6 turns in the ring is enough for finishing the phase rotation. Initial momentum spread of 68MeV/$c\pm$ 20% is reduced to $\pm$ 2%. RF voltage applied is shown in the bottom figure.

graphite and tungsten respectively are used. The factor $\varepsilon_{\pi-decay}$ was included in Monte Carlo simulation of the pion capture system. The factor $\varepsilon_{\mu-decay}$ was estimated with another Monte Carlo simulation dedicated to the FFAG phase rotation, and it is about 60%. At the time of writing, detailed studies on $\varepsilon_{dispersion}$ and ε_{FFAG} have not been completed yet, and therefore they are assumed to be 100 %.

Table 4.4: Negative Muon yields per second (Y_μ) for various target materials, pion capture magnetic fields, muon transport magnetic fields with 10^{14} protons/sec (J-PARC 40GeV, 0.67MW) and 5×10^{14} protons/sec (J-PARC 50GeV, 4.0MW). The table is for $\varepsilon_{emittance}$ of 40,000 πmm·mrad in horizontal and 6,500 πmm·mrad in vertical.

Target material	Capture field	Transport field	Muon yield for J-PARC 0.67MW	Muon yield for J-PARC 4.0MW
Graphite	16 T	4 T	1.9×10^{11}	1.1×10^{12}
	16 T	2 T	1.4×10^{11}	8.3×10^{11}
	12 T	4 T	1.4×10^{11}	8.3×10^{11}
	12 T	2 T	1.2×10^{11}	6.9×10^{11}
	8 T	4 T	1.2×10^{11}	6.9×10^{11}
	8 T	2 T	9.3×10^{10}	5.5×10^{11}
	6 T	4 T	6.9×10^{10}	4.2×10^{11}
	6 T	2 T	6.9×10^{10}	4.2×10^{11}
Tungsten	16 T	4 T	5.0×10^{11}	3.0×10^{12}
	16 T	2 T	4.2×10^{11}	2.5×10^{12}
	12 T	4 T	3.7×10^{11}	2.2×10^{12}
	12 T	2 T	3.5×10^{11}	2.1×10^{12}
	8 T	4 T	2.3×10^{11}	1.4×10^{12}
	8 T	2 T	2.8×10^{11}	1.7×10^{12}
	6 T	4 T	1.6×10^{11}	9.7×10^{11}
	6 T	2 T	1.9×10^{11}	1.1×10^{12}

Chapter 5

The PRIME Detector

5.1 Overview

In this section, we describe a candidate detector for the PRIME experiment in detail. The sole role of the detector is to select the genuine $\mu^- - e^-$ conversion signal from a huge number of background events. The signature of the $\mu^- - e^-$ conversion signal is clear, namely, a mono-energetic ($\sim$105 eV) electron coming from the muon stopping target. By contrast, background events have various origins, and are huge. We have to reject the background to reduce detector hit-rate and to identify the signal event by a spectrometer. The only way to distinguish the signals from backgrounds is to measure the electron momentum and energy as precise as possible. We expect it is necessary to achieve an energy resolution of 350 keV(FWHM) for electrons, when the branching sensitivity of 10^{-18} is to be reached. The background rejection will be explained in detail in Chapter 6.

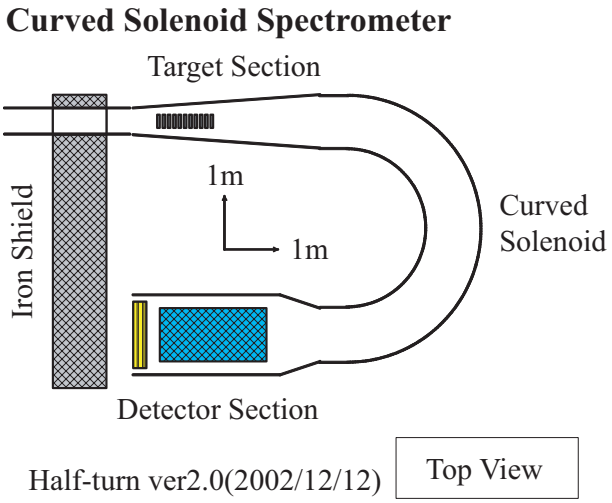

Figure 5.1: Setup of a proposed spectrometer.

One of the potential drawback of using the PRISM beam is its low duty factor.

The repetition of the PRISM beam is ∼10 pulse/cycle in the entry stage, and ∼100 pulse/cycle at its upgrade. Thus, the instantaneous beam intensity is about $10^9 \sim 10^{10}\mu^-$ per bunch for a MW proton beam power. The measurement time window opens for about a μsec. Any detector using the PRISM beam must be able to handle this instantaneous intensity. To summarize, the requirements for the detector are

1. capability of handling a very high instantaneous rate,
2. good energy resolution to distinguish the $\mu - e$ conversion signal from electrons coming from decay-in-orbit, and
3. good rejection of background events.

In the PRIME experiment, we consider to employ a curved solenoid spectrometer, which would meet the requirements listed above. As shown in Fig. 5.1, the curved solenoid spectrometer consists of three sections; a target section, a curved solenoid section, and an electron detection section. Each section will be described in detail below.

5.2 Muon Stopping Target

The muon stopping target must be designed to maximize the muon stopping efficiency and the acceptance of the $\mu^- - e^-$ conversion electron to the spectrometer. Also, it should be designed to minimize the energy loss of the $\mu^- - e^-$ conversion electron as they exit the target in order to improve the momentum resolution of the electrons. It would be also important to have the smallest possible target size to reduce any kinds of possible backgrounds.

5.2.1 Range of muons

One of the significant features of using the PRISM muon beam is to have narrow momentum spread. According to the present PRISM design, a momentum spread of ± 3 % with the central momentum of 68 MeV/c (being equivalent to 20 MeV in kinetic energy) is expected after phase rotation.

To examine a muon-stopping target needed to stop such a muon beam, Monte Carlo simulations based on GEANT3 have been done. In this particular simulations, a range of muons in Ti was examined by taking account of range straggling and multiple scattering. A preliminary result is shown in Fig. 5.2 (left), where a range width is about 380 μm in sigma. The input beam is a parallel beam whose momentum distribution is uniform in the momentum range of ± 3 % with 68 MeV/c central momentum. It implies that a Ti target of 1 mm in total thickness is sufficient to stop about 80 % of the beam muons.

The present range width is not dominated by range straggling nor multiple scattering, but dominated by the momentum distribution in the beam muons. Fig. 5.2 (right) shows range distribution as a function of muon momentum, where it is clearly seen that the muon-momentum distribution determines the total range width, and

the effects from range straggling is smaller. If the performance of phase rotation at PRISM gets better, there is still a room to get a muon-stopping target thinner by a factor of two at most (to about 500 μm full width).

Thus the stopping target configuration is critical. Major parameters to be considered are material, thickness, size (diameter), a number of layers, a distance between adjacent layers (spacing), and a magnetic field and its gradient. We have considered various target configurations. Our tentative target configuration is to use 20 layers of 50 μm thick Ti foils. The diameter of those targets is 50 mm, and they are spaced by 5 cm one another.[1]

5.2.2 Energy Loss of Outgoing Electrons

Fig. 5.3 shows a distribution of the traversed thickness for the case of the 105 MeV/c signal electrons. The events toward the upstream histogrammed on the bin at -0.001 for convenience. (The fraction of those events is about 20%, as explained above.) Fig. 5.4 shows GEANT-simulated energy loss in a 50μm Ti target for the electrons impinging normally. Several relevant numbers can be extracted from the plot; the most probable energy loss is $(\Delta E)_{mp} = 12$ keV, the median is 14 keV, and an average energy loss, excluding the largest 1% of events which are due most likely to Bremsstrahlung, is $(\Delta E)_{av}^{99\%} = 17$ keV. From these two plots, we can infer an average energy loss in the target section. For example, if we want to restrict particle's energy

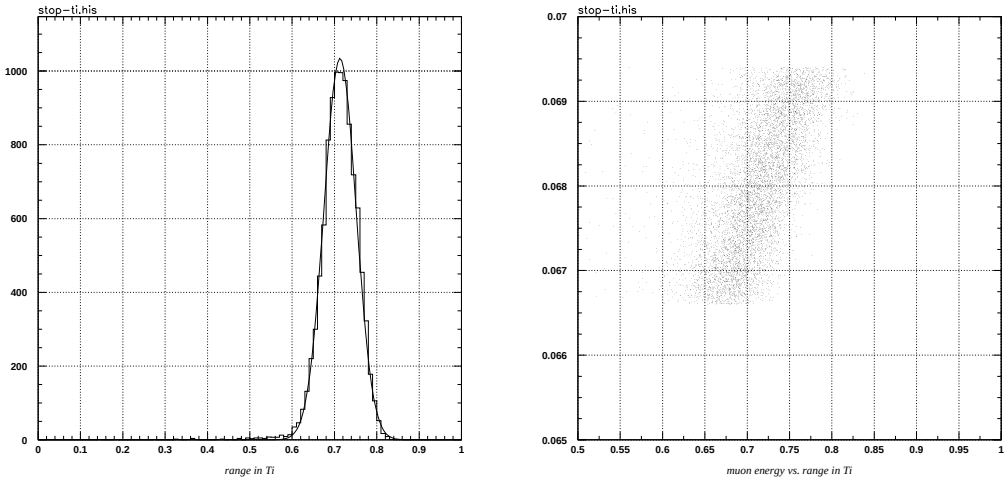

Figure 5.2: (Left) Range of muons of 68 MeV/c with ± 3 % momentum width. The range distribution is about 380 μm in sigma. (Right) 2-dimensional plot of muon momentum (vertical) vs. range (horizontal). The effects from range straggling is smaller than the momentum spread.

[1]Note that 17−25 layers of 200 μm aluminum thin disks with 5 cm separation are going to be used in the MECO experiment with about 56 % stopping efficiency.

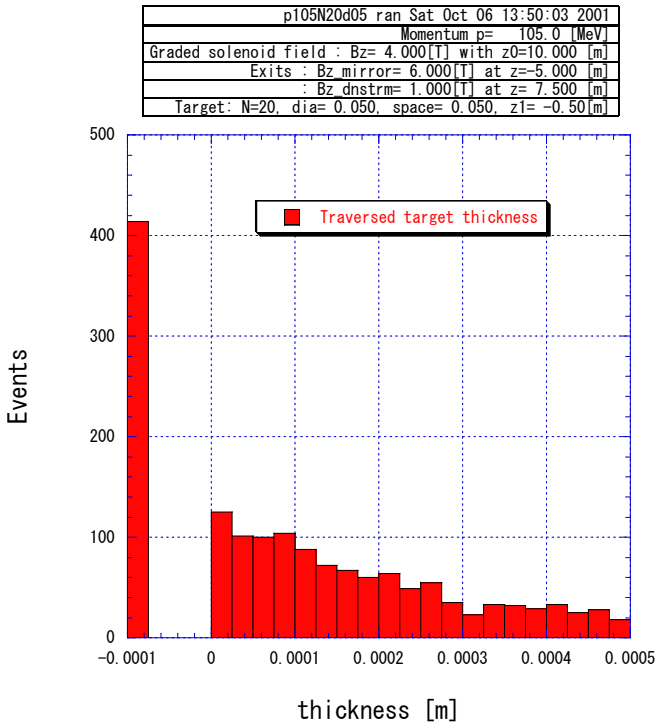

Figure 5.3: Target thickness traversed by signal electrons.

loss to be less than 150 keV, then the total thickness traversed should be 450 μm or less. Here we used $(\Delta E)_{av}^{99\%}$ in calculating the average energy loss. From Fig. 5.3, about 54.8% of particles generated in the targets go forward with $(\Delta E)_{av}^{99\%} < 150$ keV. There is no strong dependence upon the target position for those electrons.

5.3 Curved Solenoid Spectrometer

5.3.1 A Principle of Curved Solenoid Spectrometer

The curved solenoid spectrometer is a magnetic system to select a charged particle with a desired momentum. Its main features are a large acceptance and a good rejection power. In the section, we present the curved solenoid spectrometer itself, and some study results of its performance. First of all, its principle is explained. It is well known that charged particles move in a helical motion around magnetic fluxes in a solenoidal field. When the solenoid is curved, as in a toroidal field, they drift normal to the bending plane. A drift distance D is given by

$$D = \frac{1}{qB_0}\left(\frac{s}{r_0}\right)\left(\frac{p_\parallel^2 + \frac{1}{2}p_\perp^2}{p_\parallel}\right),$$

where B_0 represents a magnetic field, r_0 is a radius of the toroid, s is a path length along the particle's central orbit, and $p_\parallel(p_\perp)$ represents respectively particle's par-

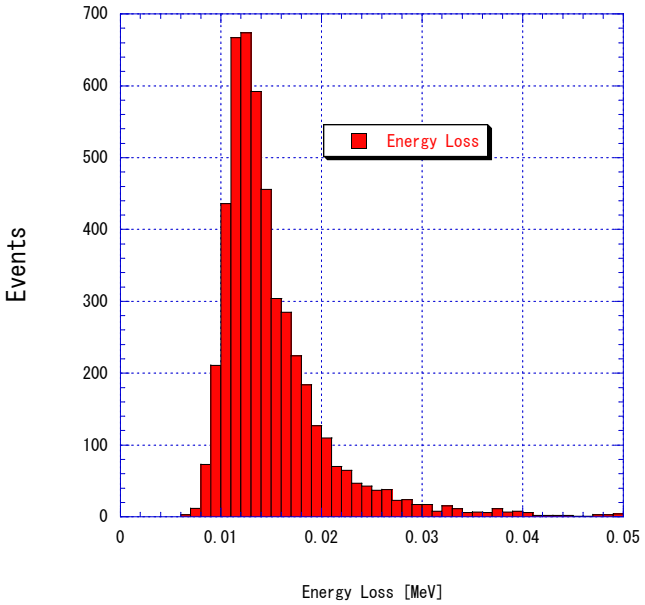

Figure 5.4: Energy loss distribution in a 50 μm-thick target.

allel (perpendicular) momenta. This drift can be compensated by an auxiliary field imposed along the drift direction. Its value is represented by

$$B_{aux} = \frac{B_0 v_{\parallel}}{\omega_B r_0}\left[1 + \frac{1}{2}\left(\frac{p_{\perp}}{p_{\parallel}}\right)^2\right]$$

with $\omega_B = qc^2 B_0/E_e$. For example, if r_0 is set to 2 m, B_{aux}=0.18 T for the signal electron with $\tan\theta = p_{\perp}/p_{\parallel} = 0$. In order to use this toroidal field as a spectrometer (or a momentum filter), it is essential to remove particle's polar angle dependence (θ). In our case, since the polar angle θ_z is less than 0.5 at the entrance, the contribution of the $\tan\theta$ term is small. Thus, this toroid field act as an efficient momentum selector, as will be shown in the next subsection.

5.3.2 Transport Efficiency

Fig.5.5 shows an example of tracks in the curved solenoid spectrometer. The track with desired momentum (105 MeV/c) stays in the same horizontal plane, thanks to the auxiliary field, although it undergoes circular motion in the solenoidal field. On the other hand, a track with a wrong momentum (85 MeV/c for example) drifts downwards. Since the vertical drift distance D depends upon particle's momentum, unwanted particles can be eliminated by placing appropriate blocker(s) in the solenoid.

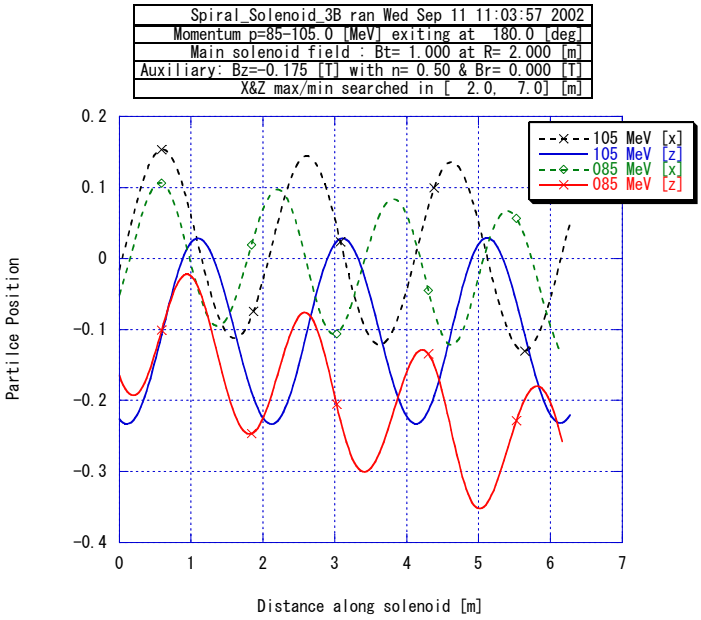

Figure 5.5: Example of tracks in the solenoid.

Fig. 5.6 shows a distribution (Z-min), the minimum drift in the Z-direction recorded in the curved section. Considering the background rate, we have decided to place a blocker that removes the particles with $Z_{min} < -0.15$ m. Fig. 5.7 shows fraction of the particles that reach the detector section as a function of their momentum. It is found that about 53 % can be tranported successfylly while keeping the background rate sufficiently low. Thus it is concluded that the curved solenoid spectrometer is quite efficient to remove unwanted particles.

5.4 Electron Detector

5.4.1 Overview

The main purpose of the electron detector is to identify electrons and to measure their energies. One example of the detector system is shown, although it is possible to be replaced by better one later.

The electron detector consists of a tracker, trigger scintillators, and an electromagnetic calorimeter. Two issues are important when considering the electron detector. The first is a number of particles par pulse entering the detector. If this number is large, the detector would not be able to distinguish the signal from backgrounds. The second is the detector energy resolution. The goal of the energy resolution is 350 keV (FWHM). Brief description for each detector component is shown in the following.

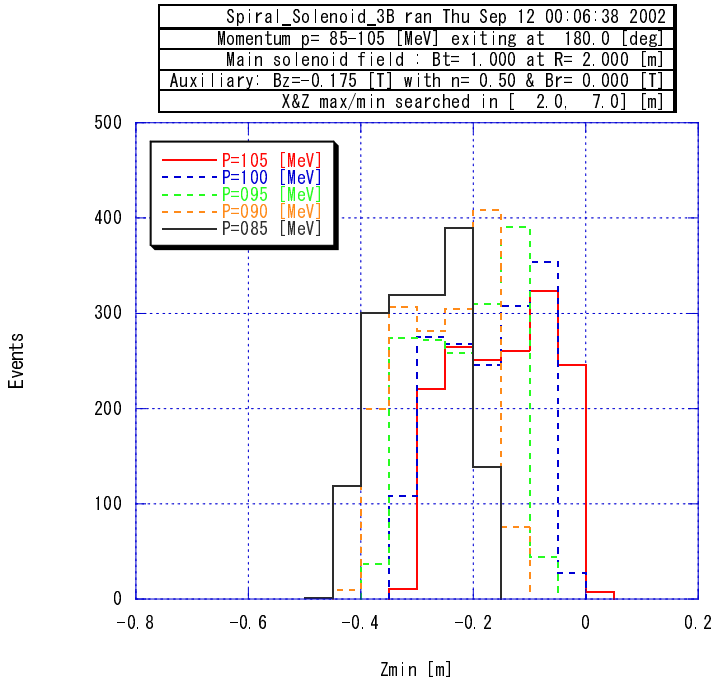

Figure 5.6: Zmin distribution in the solenoid.

5.4.2 The Tracking Detector

The tracking detector consists of multiple sets of (planer) tracking chambers (TC0-TC9). They are installed in the detector solenoid, covering the entire solenoid aperture. One candidate is a straw-tube tracking chamber of thin wall thickness, such as 25 μm. Since the momentum resolution of the tracking detector is dominated by multiple Coulomb scattering, a low mass chamber is demanded. Since the tracking detector has to be placed in vacuum, an ordinary planer chamber with a large area is difficult to install. Therefore, a straw tracking chamber is the best.

One set might consist of three layers (u, v and w) of straw tracking chambers. Each straw chamber has a 5-mm radius. To increase redundancy, a pair of sheets of cathode strips could be possibly placed upstream and downstream sides from the tracking layers. Induced charges on the cathode strips are used to determine the coordinate along the straw axis. We have already carried out an R&D of straw tracking chambers, in particular, seamless straw-tube tracking chamber, The details can be presented in the appendix. From our R&D work, an anode position resolution of 100 μm and a cathode position resolution of 250 μm were obtained.

5.4.3 The Trigger/Energy Detector

The main purpose of this trigger/energy detector is to determine precisely a timing of the track, at the same time, determine a total energy of the track. One candidate

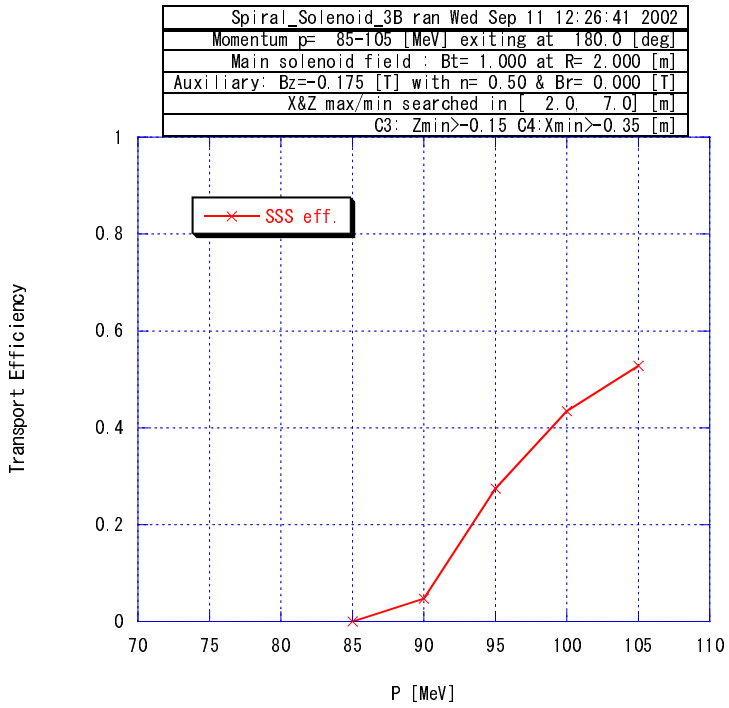

Figure 5.7: Curved solenoid transport efficiency. The cut values on Zmin and Xmin are $Zmin > -0.15$ and $Xmin > -0.35$, respectively.

is a plastic scintillator followed by either a lead-scintillator sandwich detector or an inorganic crystal detector. There will be about 5 tracks in the detector within the measurement time of 1 μsec per single burst of the muon beam pulse. Therefore, segmentation would be desired to reduce overlapping. The segmentation would also give additional hit position which would help reconstruction of the tracks. By comparing the energy (which is measured at the trigger/energy detector) and the momentum (which is measured at the tracking detector) of the tracks, the particle identification can be made.

5.4.4 Trigger and Data Acquisition System

A trigger signal to a data acquisition system is formed by the coincidence signal between the trigger counter and the electromagnetic calorimeter. Since we expect about 10 particles maximum to enter the detector, no "fast" electron is possible. All of them must be read in the DAQ computer using a pipe-line data acquisitions system.

5.4.5 Detector Rates

Complete tracks entering the detector are expected to be dominated by decay-in-orbit electrons. Positively charged particles and neutrals would be filtered out, to a large

extent, by the curved solenoid spectrometer. In order to estimate a number of the particles entering the detector section, the decay-in-orbit electron spectrum shown in the MECO proposal was used.

Convoluting this spectrum with the efficiency in Fig. 5.7, and assuming that 10^{10} muons per pulse stop and decay in the target, we have obtained a number of the particles going into the detector to be about 5, no more than 10. Considering segmentation of the tracking chambers, and the fact that these events come in a time interval of ~ 1 μsec, it is concluded that the detector could handle this rate.

5.4.6 Momentum Resolution

Monte Carlo simulations have been made to examine the momentum resolution of electrons in the spectrometer. The position resolutions of the tracking chamber are assumed to be 100 μm in xy directions. The $\mu^- - e^-$ conversion electrons of 104.3 MeV were generated uniformly at the muon-stopping target. The energy loss in the target makes a long tail in low energy. Fig. 5.8 shows the fitted momentum distribution at the spectrometer.

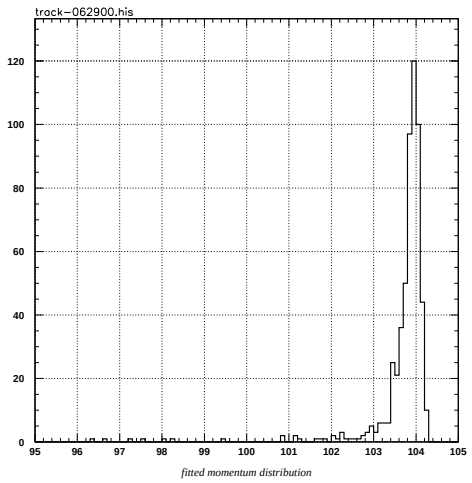

Figure 5.8: Fitted momentum distribution at the spectrometer.

To examine the intrinsic momentum resolution, difference of the fitted momentum from the true momentum at the spectrometer is shown in Fig. 5.9(a). From Fig. 5.9(a), the intrinsic momentum resolution of about 100 keV (FWHM) has been obtained. Fig. 5.9(b) shows the difference of the fitted momentum from the true momentum at birth (namely 104.3 MeV). The net momentum resolution is about 235 keV (FWHM). The net momentum resolution is dominated by the energy loss in the target.

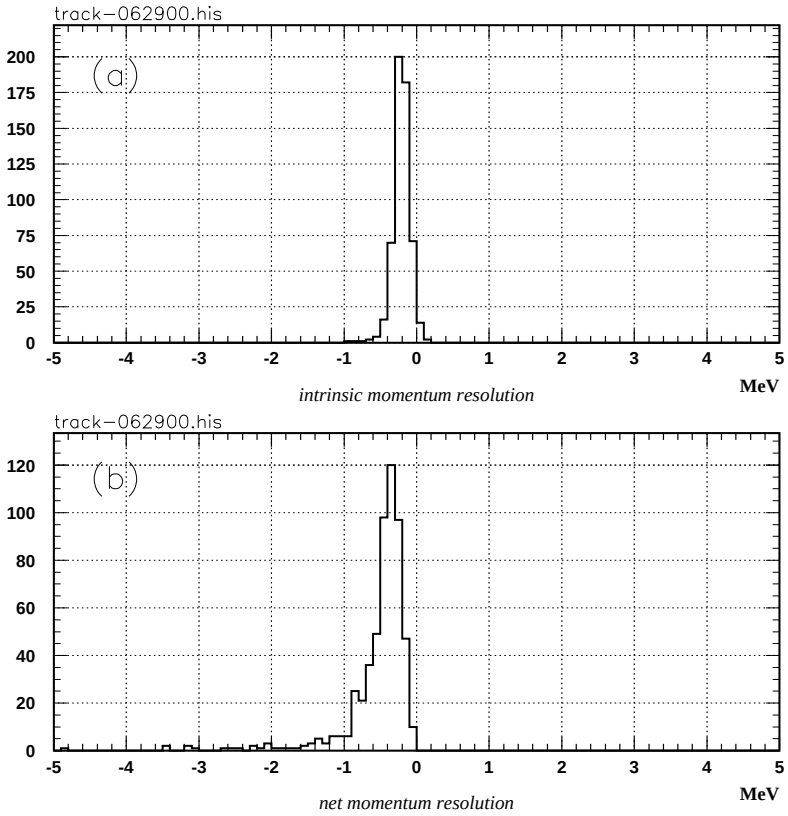

Figure 5.9: (a) Intrinsic momentum resolution at the spectrometer (100 keV FWHM) and (b) net momentum resolution with energy loss in the target (235 keV FWHM).

5.5 Detection Acceptance

The detector acceptance is estimated. The followings are considered : (1) geometrical acceptance at the target, (2) a transport efficiency of the spectrometer, and (3) requirement of particle's polar angle in the electron detector section. The other factors, which might affect the signal sensitivity, such as a stopping target efficiency, and a cut efficiency related to energy loss in the target, are not included here. Table 5.1 summarizes the results of our study. Elections will be emitted from the stopping target uniformly. Some of the electrons emitted in the backward would not come into the curved solenoid spectrometer. Due to the magnetic mirror effect, the geometrical acceptance to enter the spectrometer amounts to 80%, as was already described. The transport efficiency of the spectrometer of 53% was already described. The last item is the requirement for the electrons to have a large polar angle θ at the detector region. If the polar angle is small, the electron momentum would not be analyzed with sufficient resolution since a radius of the helix becomes too small to be measured. We placed a condition to the electron's polar angle θ being $\sin\theta > 0.33$, which corre-

sponds to $p_t > 86$ MeV/c for the signal electron at the target region. This requirement results in the acceptance of 80%. Multiplying these factors, we have obtained 35% for a net of geometrical acceptance.

Table 5.1: Geometrical acceptance of the proposed spectrometer.

Condition	Section	Fraction	Net acceptance	Remark
Forward direction.	target	79.3%	79.3%	
Blocker cut (vertical)	curved solenoid	53.0%	42.0%	Zmin>-0.15
Blocker cut (horizontal)	curved solenoid	100%	42.0%	Xmin>-0.35
$\sin\theta > 0.33$	detector	82.3%	34.6%	

Chapter 6

Signal and Backgrounds

6.1 Signal Sensitivity

In this section, we estimate the signal sensitivity to search for a $\mu^- - e^-$ conversion process in the PRIME detector. A single event sensitivity is defined by a number of muons stopping in the target and the detector acceptance, as follows.

$$B(\mu^- + Ti \rightarrow e^- + Ti) \sim \frac{1}{N_\mu \cdot A_\mu}, \tag{6.1}$$

where N_μ is a total number of muons stopping in the target and A_μ is the detector acceptance.

The muon yield is estimated to be about $10^{11} - 10^{12}$ muons/sec by the PRISM muon source, depending on the technology adopted, as described in Section 4.6. The contributions to the acceptance A_μ are summarized in Table 6.1. The net detection acceptance of our apparatus can be estimated to be 0.22, where the analysis efficiency is assumed to be 0.8, assuming the electron energy cut above 104.1 MeV to reject background events as described in Section 6.

Table 6.1: Acceptance of each section in PRIME.

Items	Acceptance
Muon Stopping efficiency	0.8
Acceptance of the spectro-meter	0.8
Transport efficiency of the curved solenoid	0.53
Kinematic acceptance of PRIME detector	0.8
Analysis cut	0.8
Total	0.22

By using the detector acceptance and the muon yield estimated by the previous

sections, the single event sensitivity for PRIME is estimated as[1]

$$B(\mu^- + Ti \rightarrow e^- + Ti) \sim 6 \times 10^{-19}. \tag{6.2}$$

Since a 90 % confidence level upper limit is given by $2.3/(N_\mu \cdot A_\mu)$, the upper limit is obtained as

$$B(\mu^- + Ti \rightarrow e^- + Ti) < 10^{-18} \quad (90\% \text{ C.L.}), \tag{6.3}$$

which is about 10^6 times better than the current published limit obtained by SINDRUM II at PSI.

6.2 Background Rejection

It is useful to categorize background events. One type is a so-called "intrinsic background", which stems from $\mu^- - e^-$ decays in orbit. For a Ti target, about 15% of the muons bounded in an atomic orbit end up with this process. The energy spectrum of the ejected electrons resembles the Michel spectrum. But, due to nuclear recoil, its high energy tail extends up to the energy of the signal. The only way to distinguish the signal from this type of background is to measure the electron energy as precise as possible. The signal, if it exists, would stand up as a peak over the decay-in-orbit background spectrum. We expect it necessary to achieve an energy resolution of 350 keV(FWHM) when the branching sensitivity of 10^{-18} is to be reached.

Other types of background events come from various sources: $\pi^-/\bar{p}$ capture or scattering of electrons in the targets, and cosmic rays, etc. Generally speaking, the energy spectrum of these backgrounds is broad and spreads over the signal energy region. Rejection of these backgrounds must be individually considered. In our experiment, the backgrounds due to $\pi^-/\bar{p}$ captures can to be reduced to a negligible level by reducing their contaminations in the beam. The background events due to cosmic rays can be decreased by active and/or passive shields. In addition, the duty factor of the PRISM beam makes the cosmic ray events smaller. The electron scattering events can be safely neglected if the electron energy in the beam is less than the signal energy. Since the highest electron energy comes from a muon decay in the forward direction, the muon momentum should be less than 77 MeV/c. On the other hand, the muon beam momentum from PRISM is expected to be 68 ± 2 MeV/c, which is well below the 77 MeV/c and thus the electron scattering background might be negligibly small.

Thus, the potential background sources to a search for $\mu^- - e^-$ conversion are categorized as follows; (1) intrinsic Physics Backgrounds, (2) beam-related Prompt Backgrounds, (3) cosmic ray background. In this section, the background estimations for the PRIME experiment are presented.

[1] As an example, for this estimation, the muon yield of 1.9×10^{11} muons/sec for Tungsten target under a 6 Tesla magnetic field for 5-year running period is used.

6.2.1 Intrinsic Physics Backgrounds

6.2.1.1 Muon Decay in Orbit

Muon decays in orbit (DIO) are one of the important background sources in the search for $\mu^- - e^-$ conversion in a muonic atom, since the end point of the DIO electron spectrum comes close to the signal region of $\mu^- - e^-$ conversion. We have estimated the background rate from a muon decay in orbit by using the theoretical calculation. If the signal region is determined above 104.1 MeV with the energy resolution of 350 keV (FWHM) we have about 0.01 background events at a sensitivity of 10^{-18}.

6.2.1.2 Radiative Muon Capture

Radiative muon capture (RMC), $\mu^- + (A, Z) \rightarrow \nu_\mu + (A, Z-1) + \gamma$, followed by asymmetric e^+e^- conversion of the photon is another background source. For the MC simulation, the energy spectrum of the RMC γ is evaluated by using the experimental data available, which is fitted by Primakoff's formula [42]. By the procedure, the maximum energy of the RMC γ ($E_{\rm max}^{\rm RMC}$) is estimated as 89.2 MeV for Ti. Since $E_{\mu e}$ is 104.3 MeV, $E_{\rm max}^{\rm RMC}$ is enough apart from $E_{\mu e}$ (about 100 σ with the energy resolution of 350 keV (FWHM)). Therefore, the contamination of RMC into the signal region above 104.1 MeV is negligible level.

6.2.2 Beam-related Prompt Backgrounds

6.2.2.1 Radiative Pion Capture

The radiative pion capture (RPC), $\pi^- + (A, Z) \rightarrow (A, Z-1) + \gamma$, followed by internal and external asymmetric e^+e^- conversion of the photon ($\gamma \rightarrow e^+e^-$) could be the most serious source of the background. In the PRIME experiment, all the charge particles are forced to travel about 150 m in the PRISM FFAG ring. Since the mean flight length of pions ($= \beta\gamma\tau_\pi c$) is about 4 m, only a fraction of 3×10^{-17} of pions will survive and enters to the PRIME detector. Thus, the expected number of this background events is estimated to be about 10^{-3} events at the sensitivity of 10^{-18}.

6.2.2.2 Beam Electrons

If electrons in a beam are scattered at the muon stopping target into the detector, they might become background events. The FFAG ring only accepts electrons with their momentum below 85 MeV/c. As discussed in the previous section, about 10^{-18} pions per one 50 GeV proton on the production target is survived after FFAG ring. Those pions can generate with the probablity of about 5×10^{-6} daughter electrons with their energy above 102 MeV and $p_t > 90$ MeV/c. By using the probability, the background contamination would be estimated as 0.008.

6.2.3 Cosmic Ray Backgrounds

The cosmic ray induced backgrounds can be reduced significantly by a duty factor of the PRIME detection period, in addition to both active and passive cosmic ray shielding. By the simple estimation, the background rate at PRISM is estimated as about 3×10^{-7} events per 10^7 seconds.

6.2.4 Summary of Background Rates

The expected background rates for PRIME at a sensitivity 10^{-18} is summarized in Table 6.2 . This shows that the background rates would be sufficiently small.

Table 6.2: Estimated background rates for PRIME at a signal sensitivity of 10^{-18}.

Background	Events
Muon decay in orbit	0.01
Radiative muon capture	negligibly small
Radiative pion capture	10^{-3}
Beam electrons	0.008
Cosmic rays	10^{-7}
Total	0.02

Chapter 7

A Pulsed Proton Beam for PRISM/PRIME at J-PARC

In order to proceed the PRISM/PRIME experiment, a pulsed proton beam is definitely necessary as mentioned in Chapter 4. The current plan of J-PARC has a neutrino facility (for T2K) which will use a pulsed proton beam. However, it dose not have capability to accommodate any other experiment due to space limitation. Therefore, we proposed and requested another pulsed proton facility for muons. A

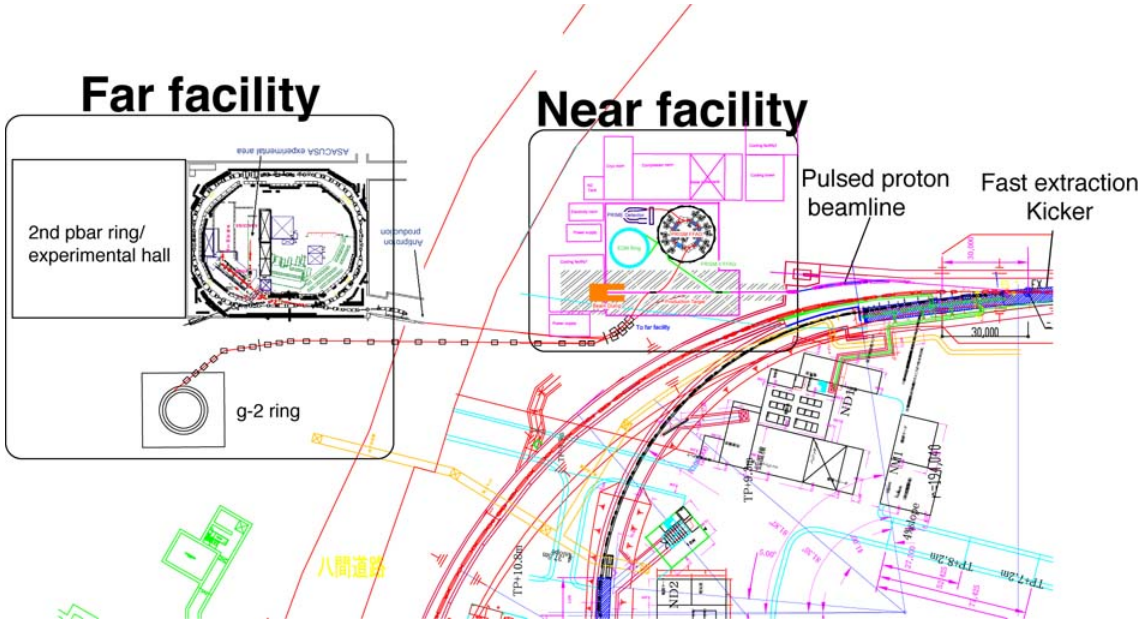

Figure 7.1: A schematic layout of the proposed pulsed proton facility that consists of the near and far facilities.

proposed layout of the pulsed proton facility is presented in Fig.7.1. A possible location will be north from the 50-GeV PS ring tunnel close to the planned beam-abort dump. Proton bunches in the 50-GeV ring are kicked off outside with respect to the 50-GeV tunnel. The facility consists of a near facility, which include PRISM, and a far facility.

Fig.7.2 shows a possible layout of the near facility, which consists of production targets (for pions/muons and antiprotons), a full beam dump, and an experimental hall. PRISM and PRISM-II (of muons of 500 MeV/c for the measurement of the muon electric dipole moment (EDM)) will be located in this hall.

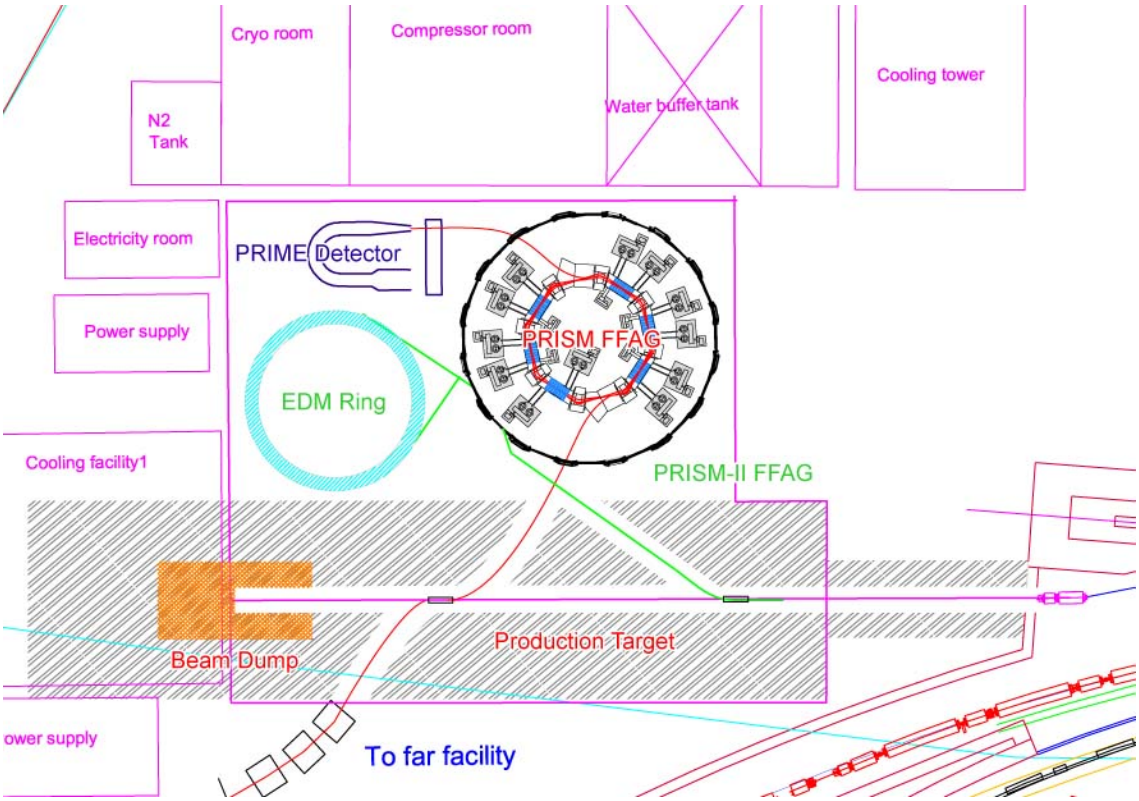

Figure 7.2: A schematic layout of the Near Facility. PRISM-FFAG, PRISM-II-FFAG and EDM ring are installed.

Chapter 8

Conclusion

We, the PRISM/PRIME working group, would like to continue expressing our interest to initiate a search for the $\mu^- - e^-$ conversion process in a muonic atom towards an ultimate sensitivity of 10^{-18}. Charged lepton flavor violation, in particular in the muon system, is one of the most important subjects in particle physics. It has large discovery potential to find new physics beyond the Standard Model. Especially, it is sensitive to supersymmetric extension to the Standard Model. The sensitivity proposed would cover the most of parameter spaces in supersymmetric grand unification models and the minimal standard model with the seesaw mechanism.

To carry out search for $\mu^- - e^-$ conversion processes, where a single electron of its energy of 104.3 MeV is detected, the quality of muon beam is the most important. Thus we have proposed to construct a high intensity low-energy muon source called PRISM (= Phase Rotated Intense Slow Muon source). It has a narrow energy spread and no pion contamination. These features are of critical importance. We confidently show that the search for $\mu^- - e^-$ conversion process at a sensitivity of 10^{-18} with sufficiently small background rates can be accomplished. We are also confident that a great discovery can be made with PRISM/PRIME.

Bibliography

[1] Kuno Y and Okada Y, Review of Modern Physics, **73** (2001) 151.

[2] Hincks E P and Pontecorvo B 1947 *Phys. Rev. Lett.* **73** 246

[3] Brooks M L *et al.* (MEGA Collaboration) 1999 *Phys. Rev. Lett.* **83** 1521–1524

[4] Bellgardt U *et al.* 1988 *Nucl. Phys.* B **229** 1

[5] Wintz P 1998 in *Proceedings of the First International Symposium on Lepton and Baryon Number Violation*, edited by H.V. Klapdor-Kleingrothaus and I.V. Krivosheina (Institute of Physics Publishing, Bristol and Philadelphia), p.534

[6] Willmann L *et al.* 1999 *Phys. Rev. Lett.* **82**, 49

[7] K. Hayasaka *et al.* (Belle Collaboration) 2005 *Phys. Lett.* B **613**, 20

[8] K. Abe *et al.* (Belle Collaboration) 2004 *Phys. Rev. Lett.* **92**, 171802

[9] B. Aubert *et al.* (BaBar Collaboration) 2004 *Phys. Rev. Lett.* **92** 121801

[10] Krolak P *et al.* 1994 *Phys. Lett.* B **320**, 407.

[11] Ambrose D *et al.* (BNL E871 Collaboration) 1998 *Phys. Rev. Lett.* **81** 5734

[12] Lee A M *et al.* 1990 *Phys. Rev. Lett.* **64**, 165.

[13] Arisaka K *et al.* 1998 *Phys. Lett.* B **432**, 230.

[14] Akers R *et al.* (OPAL Collaboration) 1995 *Z. Phys.* C **67**, 555

[15] Abreu P *et al.* (DELPHI Collaboration) 1997 *Z. Phys.* C **73**, 243

[16] Hall L J, Kostelecky V A and Raby S 1986 *Nuclear Physics* B **267** 415–432

[17] Barbieri R, Hall L and Strumia A 1995 *Nuclear Physics* B **445** 219–251

[18] Hisano J, Moroi T, Tobe K, and Yamaguchi M 1997 *Phys. Lett.* B **391** 341–350; Erratum 1997 *Physics Letters* B **397** 357

[19] Hisano J, Moroi T, Tobe T, Yamaguchi M, and Yanagida T 1995 *Phys. Lett.* B **357** 576

[20] Hisano J, Nomura D, and Yanagida T 1998 *Physics Letters* B **437** 351

[21] Hisano J and Nomura D 1999 *Phys. Rev.* D **59** 116005

[22] Kosmas T S, Faessler A and Vergados J D 1997 *J. Phys. G* **23** 693–703 : Kosmas T S and Vargados J D 1996 *Phys. Rep.* **264** 251–266 : Shanker O 1979 *Physics Review* D **20** 1608–1615

[23] Czarnechi A, Marciano W J and Melnikov K 1998 *Coherent Muon-Electron Conversion in Muonic Atoms* Preprint BNL-HET-98/2, TTP 97-19, hep-ph/9801218

[24] Raidal M and Santamaria A 1998 *Phys. Lett.* B **421** 250–258

[25] Weinberg S and Feinberg G 1959 *Phys. Rev. Lett.* **3** 111; **3** 244(E)

[26] Marciano W J and Sanda A I 1977 *Phys. Rev. Lett.* **38** 1512

[27] Kitano R, Koike M and Okada Y 2002 *Detailed calculation of lepton flavor violating muon-electron conversion rate for various nuclei* Preprint KEK-TH-808, hep-ph/0203110

[28] Honecker W *et al.* (SINDRUM II Collaboration) 1996 *Phys. Rev. Lett.* **76** 200

[29] Bachman M *et al.* 1997, a research proposal to Brookhaven National Laboratory AGS "A Search for $\mu^- N \to e^- N$ with Sensitivity Below 10^{-16}, **M**uon – **E**lectron **CO**nversion"

[30] Dzhilkibaev R M and Lobashev V M 1989 *Sov. J. Nucl. Phys.* **49** 384

[31] Bryman D A, Blecher M, Gotow K and Powers R J 1972 *Phys. Rev. Lett.* **28** 1469

[32] Badertscher A *et al.* 1982 *Nucl. Phys.* A **377** 406

[33] Bryman D A *et al.* 1985 *Phys. Rev. Lett.* **55** 465

[34] Ahmad S *et al.* 1988 *Phys. Rev.* D **38** 2102

[35] Dohmen C *et al.* (SINDRUM II Collaboration) 1993 *Phys. Lett.* B **317** 631

[36] Barkov L M *et al.* 1999, a research proposal to PSI "Search for $\mu^+ \to e^+\gamma$ down to 10^{-14} branching ratio"

[37] Kuno Y *et al.* 1998 in *Proceedings of Workshop on High Intensity Secondary Beam with Phase Rotation* edited by Y. Kuno and N. Sasao p.71

[38] J.D. Jackson "Classical Electro Dynamics", third edition, John Wiley & Sons, Inc. (1998)

[39] Shanker O 1982 *Phys. Rev.* D **25** 1847

[40] Hänggi P, Viollier R D, Raff U nd Adler K 1974 *Phys. Lett.* **51B** 119

[41] Herzog F and Adler K 1980 *Helv. Phys. Acta* **53** 53

[42] Primakoff H 1959 *Rev. Mod. Phys.* **31** 802

[43] Armstrong D S *et al.* 1992 *Phys. Rev.* C **46** 1094

[44] Kaulard J *et al.* 1998 *Phys. Lett.* B **422** 334

[45] Doornbos J "Considerations for a proton beam line to the PRISM target at J-PARC", internal note (2005)

Appendix A

PRISM FFAG Ring R&D

A.1 Introduction

One of the key apparatus in PRISM is a phase rotator which make beam energy spread narrower. The phase rotator in PRISM may have the following requirements;

- rapid acceleration / deceleration,
- large transverse acceptance, and
- large momentum acceptance.

As a phase rotator, a fixed field alternating gradient synchrotron (FFAG) has been adopted.

A scaled-radial-sector-type FFAG with triplet focusing was decided to use. This type has a magnet whose entrance and exit faces are on the radial line drawn from the machine center. There are normal and reverse bending magnets with nonlinear gradient, which provide focus and defocus property in each transverse plane. Focusing and defocusing actions comes also from an angle between the entrance and exit orbits and the magnet face. This configuration has advantages that the field clamp effects which is expected between the adjacent focusing defocusing magnet and each straight section becomes larger, compared to the separated function configuration.

A.2 Lattice design

Lattice of cyclic accelerators is usually designed by a simulation codes so called MAD, SAD, etc, or, by tracking simulation by using 3D magnetic field calculated by TOSCA. However in former methods, it is difficult to include fringing magnetic field into the codes, in latter method, it take a long time to produce a 3D map of the magnetic field. To overcome these problem, a unique method has been developped. In this method, 3D field map is prodeced by interpolating a 2D field map calculated by POISSON. It take a only 10 minutes to produce a 3D field map on the other hand, it take a several hours in TOSCA method. With this method, the optimum lattice parameters has been determined. The lattice parameters are tablated in Table A.1.

Parameters	values
number of cells	10
field index (k)	4.6
aperture	30 cm × 100 cm
average radius	6.5m
F/D ratio	6
F/2 angle	2.2 degree
D angle	1.1 degree

Table A.1: Lattice parameters of PRISM-FFAG

A.3 Magnet Field Calculation

A cross-sectional view of the magnets on its median plane is shown in Fig. A.1. The triplet magnet consists of one focusing (F) magnet, two defocusing (D) magnets, and two field clamps which reduce a fringing magnetic field at the location of RF cavities to avoid field saturation inside the RF cores. The F and D poles are magnetically short-circuited by the common top iron poles. This configuration make reduction of magnetic flux density in its return yoke. At the same time, a total yoke weight can be reduced, and in fact, it can be reduced by 30%, compared to the separated magnets.

For a radial-sector-scaling FFAG, the distribution of a magnetic field is given by

$$B(r) = B_0(\frac{r}{r_0})^k, \tag{A.1}$$

where r is the distance from the machine center to the equilibrium orbit and k is a field index. The magnetic field distribution mentioned above can be created by pole shapes, which change the gap distance inversely proportional to $B(r)$. But, in a practical design, since the F and D poles are placed closed to each other and some amount of the magnetic fluxes flow from the F pole to the D pole, the pole shape has to be adjusted by numerical calculation so as to obtain an ideal magnetic field distribution on the median plane. In Fig A.2, a cross sectional view of the F magnet is shown. The aperture size of the magnet is 30 cm in vertical and 100 cm in horizontal. Eight trim coils are installed just below the main pole. The trim coils are necessary to change the field index of the FFAG magnet field, and also to correct for possible field errors, which can be caused by, for instance, misalignment of the magnets, or piece to piece variation for the BH curve of the yoke iron material, etc. To make smooth magnetic field distribution, it is necessary to increase a number of the trim coils as many as possible. However, it leads to high cost. To avoid this and have smooth field distribution, flat plate conductors are used for each trim coils, instead of wires. The flat conductors reduce the fluctuation of magnetic field even if the coil number is little.

The magnets have shunt yokes at the radially-inside of the magnet and an open aperture at the radially-outside. This allows us to have a muon beam injected or extracted radially outside of the FFAG ring.

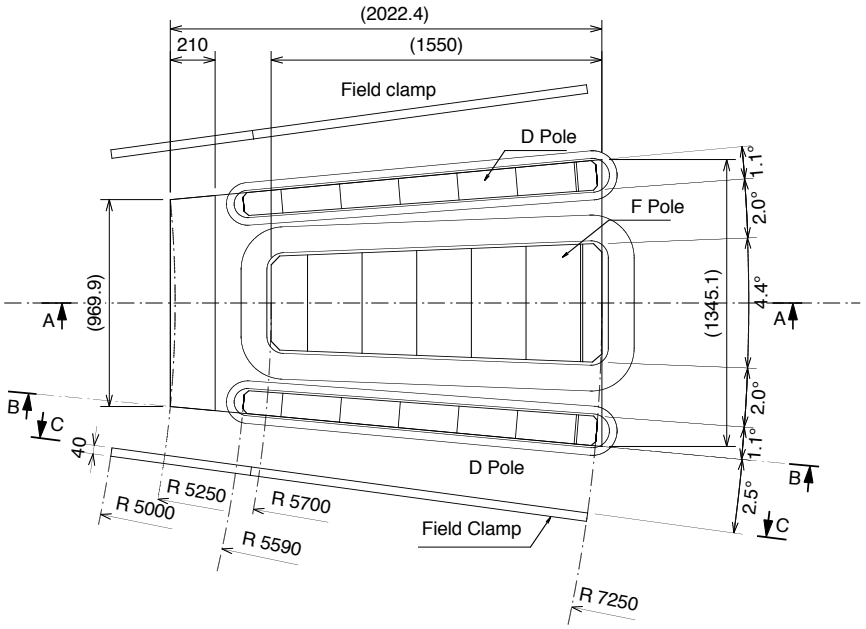

Figure A.1: The cross sectional view of the PRISM-FFAG magnet on a median plane.

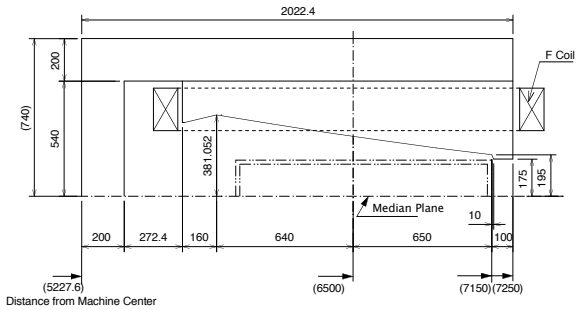

Figure A.2: A-A cross sectional view. (F Pole)

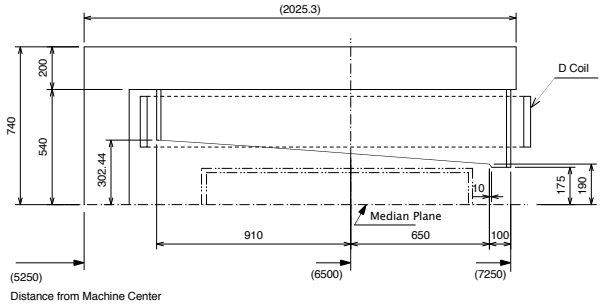

Figure A.3: B-B view. (D Pole)

A.4 Magnet design

The magnet is designed with the 3D magnetic filed analysis code, TOSCA (Vector Fields LTD Co.). The optimization is performed iteratively by changing the pole shape and the main coil currents so that the field-index k value, the magnetic field

density B_z, and the F/D ratio on the median plane, could have constant values over the magnet aperture.

Since the magnetic field is not sharply dropped to zero at the boundary, we use the BL integral, which is a integrated magnetic flux density along the circular path centered on the machine center. BL integral is given by

$$B_F L(r) = \int B_z(r)|_{B_z(r)>0} r d\theta \quad \text{(Focus)}, \tag{A.2}$$

$$B_D L(r) = \int B_z(r)|_{B_z(r)<0} r d\theta \quad \text{(Defocus)}. \tag{A.3}$$

Using the BL integral, the k value and the F/D ratio can be defined by,

$$k+1 = \frac{\partial BL(r)}{\partial r}\frac{r}{BL(r)}, \tag{A.4}$$

$$F/D = B_F L(r)/B_D L(r). \tag{A.5}$$

The target values of these parameters, which are determined by lattice studies, are shown in table A.2.

Parameters	values
field index $(k+1)$	5.6
aperture	30 cm × 100 cm
average radius	6.5m
$B_F L$ at $r = 6.5$ m	0.0855 T·m/half cell
$B_D L$ at $r = 6.5$ m	0.0143 T·m/half cell
F/D ratio	6
F/2 angle	2.2 degree
D angle	1.1 degree

Table A.2: Target parameters of PRISM-FFAG magnet